SANDIA REPORT
SAND2010-8443
Unlimited Release
Printed December 2010

Atomic Magnetometer for Human Magnetoencephalograpy

Peter D.D. Schwindt, Cort Nolan Johnson

Prepared by
Sandia National Laboratories
Albuquerque, New Mexico 87185 and Livermore, California 94550

Sandia National Laboratories is a multi-program laboratory managed and operated by Sandia Corporation, a wholly owned subsidiary of Lockheed Martin Corporation, for the U.S. Department of Energy's National Nuclear Security Administration under contract DE-AC04-94AL85000.

Issued by Sandia National Laboratories, operated for the United States Department of Energy by Sandia Corporation.

Available to DOE and DOE contractors from
U.S. Department of Energy
Office of Scientific and Technical Information
P.O. Box 62
Oak Ridge, TN 37831

Telephone: (865) 576-8401
Facsimile: (865) 576-5728
E-Mail: reports@adonis.osti.gov
Online ordering: http://www.osti.gov/bridge

Available to the public from
U.S. Department of Commerce
National Technical Information Service
5285 Port Royal Rd.
Springfield, VA 22161

Telephone: (800) 553-6847
Facsimile: (703) 605-6900
E-Mail: orders@ntis.fedworld.gov
Online order: http://www.ntis.gov/help/ordermethods.asp?loc=7-4-0#online

SAND2010-8443
Unlimited Release
Printed December 2010

Atomic Magnetometer for Human Magnetoencephalography

Peter Schwindt, Cort Johnson
Photonic Microsystems Technologies
Sandia National Laboratories
P.O. Box 5800
Albuquerque, New Mexico 87185-MS1082

Abstract

We have developed a high sensitivity (<5 fTesla/√Hz), fiber-optically coupled magnetometer to detect magnetic fields produced by the human brain. This is the first demonstration of a noncryogenic sensor that could replace cryogenic superconducting quantum interference device (SQUID) magnetometers in magnetoencephalography (MEG) and is an important advance in realizing cost-effective MEG. Within the sensor, a rubidium vapor is optically pumped with 795 laser light while field-induced optical rotations are measured with 780 nm laser light. Both beams share a single optical axis to maximize simplicity and compactness. In collaboration with neuroscientists at The Mind Research Network in Albuquerque, NM, the evoked responses resulting from median nerve and auditory stimulation were recorded with the atomic magnetometer and a commercial SQUID-based MEG system with signals comparing favorably. Multi-sensor operation has been demonstrated with two AMs placed on opposite sides of the head. Straightforward miniaturization would enable high-density sensor arrays for whole-head magnetoencephalography.

ACKNOWLEDGEMENTS

The authors wish to thank our collaborator, Dr. Michael Weisend of The Mind Research Network, for sharing his invaluable neuroscience and magnetoencephalography expertise throughout this project. The authors also wish to thank M. Romalis and V. Shah for useful discussions, M. Schendel and K. Paulson for assistance at MRN, M. Pack for field cancellation coil design, J. Bryan for electronics design and layout, and G. Burns for multifaceted technical assistance.

This project was supported by Laboratory Directed Research and Development, Sandia National Laboratories, U.S. Department of Energy, under contract DE-AC04-94AL85000, as LDRD Project Number 117842 "Atomic Magnetometer for Human Magnetoencephalography". The selection for funding by the New Directions, Cognitive Science and Technology Investment Area is gratefully acknowledged.

CONTENTS

1. Introduction 7
1.1 Magnetoencephalography: Cost and Size Reduction via Atomic Magnetometers 7
1.2 Atomic Magnetometer Basics 8
2. Potassium Free-space Magnetometer 11
3. Rubidium fiber-coupled magnetometer design/testing 15
3.1 Two-color pump probe magnetometer design 15
3.2 Sensitivity Measurements 18
3.3 Protection of Human Subjects 20
4. Human Subjects Measurements 21
4.1 Experimental Setup at The Mind Research Network 21
4.2 Single Sensor MEG measurements 23
4.3 Multiple Sensor MEG measurements 27
5. Summary and Conclusions 38
References 39
Distribution 40

FIGURES

Figure 1: (a) Neural currents produce extremely small magnetic fields (~100 fT at the scalp). (b) Highly sensitive magnetometers arrayed around the head detect these fields with millisecond resolution. The system pictured employs ~300 SQUID sensors that must be cryogenically cooled by 4K liquid helium. (c) Based upon the measured fields, neural currents can be located with sub-centimeter resolution. MEG results (yellow lines) are superimposed on an MRI scan of the brain. 8
Figure 2: Principle of operation of an atomic magnetometer 9
Figure 3: Schematic of potassium research magnetometer. 12
Figure 4. Drawing of the four-layer magnetic shield. 12
Figure 5. A drawing (a) and a photo (c) of the coil form and oven which is inserted inside the shield. A drawing (b) and a photo (d) of the oven for the potassium vapor cell. The drawing shows the vacuum tubes through which the lasers propagate. 13
Figure 6: Potassium magnetometer normalized frequency response (a) and sensitivity (b) as a function of frequency. The sensitivity plot shows how subtracting two channels can eliminate common mode noise to show the intrinsic sensitivity of each channel. Note that the red trace should be divided by a factor of $2^{1/2}$ to indicate the noise of a single channel. The green line is the photon shot noise limit of the magnetometer. 14
Figure 7: Noise spectra from two subtracted photodiodes. 14
Figure 8: Schematic of Sandia MEG magnetometer design 16
Figure 9: Photograph of the assembled magnetometer and a rubidium vapor cell. Tape measure units are inches. The optical mounts and mechanical support structure are machined from G-10 garolite fiberglass-epoxy composite. 17

Figure 10: MEG sensor sensitivity between 5-100 Hz. 19
Figure 11: Calculating the horizontal gradient from the quadrant photodiode signals. 19
Figure 12: Photograph of the magnetometer mounted inside the vacuum vessel. Tape measure units are inches. The length of the vacuum vessel provides excess interior space for routing of the fiber optic cable and electrical wires and could be substantially reduced. The holes visible on the top surface of the vacuum vessel assist in assembly and are sealed prior to evacuation. 20
Figure 13: Geometry of the 18 coil system. There are 16 square-shaped coils wrapped on the surface of cylinder, one circular coil wrapped around the center of the cylinder, and another circular coil spaced outside of the main cylinder. Listed dimensions are relative to radius of the large coil. 21
Figure 14: Human subject preparing for MEG measurements at The Mind Research Network. 22
Figure 15: Field orientations measured by an atomic magnetometer [AM, Part (a)] and a SQUID sensor [Part (b)]. 23
Figure 16: MEG signals recorded by the four-channel atomic magnetometer (AM) and four Elekta SQUID magnetometers located near the AM position. Plot a(b) shows the average evoked response from 320(110) auditory stimuli for the AM(SQUIDs). Plot c(d) shows the average evoked response from 368(313) median nerve stimuli for the AM(SQUIDs). Stimuli were applied at t = 0 s. Grey vertical lines indicate important evoked responses commonly used in MEG studies. Because the sensors measure different field components, the signal strength is not expected to be identical. However, the temporal profiles are comparable. 24
Figure 17: MEG signals from orthogonal field components. "Vertical" fields are measured by modulating in the radial direction of the coil system. Due to coil geometry, the modulation is weaker than in the "horizontal" direction (along the coil system axis), resulting in a smaller signal-to-noise ratio for the "vertical" field component. 25
Figure 18: Measured single channel sensitivity at Sandia and MRN 26
Figure 19: Contour plot of the magnitude of the magnetic field in the plane of the large and small coil pair. The white lines show the positions of the coils. The dimensions of the axes are in millimeters. 28
Figure 21: Comparison of raw data from both sensors, the principal component found using both sensors' data, and single channel data with principal component removed. 31
Figure 22: Data taken with no subject in MEG apparatus. The field sensitivity axis is horizontal and auditory tones of 2000 Hz were presented at the sensors. 32
Figure 23: Median nerve data taken in both horizontal and vertical sensitivity modes; electrode arranged to produce no wrist twitch on human subject. 32
Figure 24: Auditory data for Subject 1 for 1000 Hz and 2000 Hz tones in both the vertical and horizontal sensitive axis configurations. 33
Figure 25: Auditory data for Subject 2. 34
Figure 26: Auditory data for Subject 3. 35
Figure 27: Somatosensory data for Subject 1 36
Figure 28: Somatosensory data for Subject 2 37

1. INTRODUCTION

1.1 Magnetoencephalography: Cost and Size Reduction via Atomic Magnetometers

Functional neuroimaging is critical to our understanding of brain function and has emerged as an important technique in the diagnosis and treatment of many psychiatric and neurological disorders, such as, traumatic brain injury, schizophrenia, dementia, depression, and epilepsy. In these cases, anatomical imaging can be negative or show only nonspecific findings, and the core of the disorder or injury may lie in the functional status of or functional connections among networks of brain areas. The development of low-cost brain imaging systems would empower more researchers and clinicians with the tools necessary to these treat neurological disorders and to gain new understanding of brain function. One common modality, magnetoencephalography (MEG), directly measures the magnetic field produced by neuronal currents via an array of magnetometers arranged around the surface of the skull (see Figure 1). Despite its unique ability among neuroimaging techniques to localize neural currents with sub-centimeter spatial and millisecond temporal resolution (Hämäläinen, Hari et al. 1993) the potential of MEG as a research and clinical tool has yet to be realized due in large part to limited availability of hardware and expertise. The high cost of MEG systems is a likely contributor to the limited availability of instruments. The goal of this project has been to develop low-cost magnetometer technologies suitable for MEG.

The fields produced by the brain are extremely weak at the surface of the scalp, $< 10^{-12}$ Tesla, or approximately seven orders of magnitude smaller than the earth's magnetic field. As a result, the magnetometers in the MEG array must be extremely sensitive. Historically, the only sensors sufficiently sensitive for MEG have been superconducting quantum interference device (SQUID) magnetometers which operate at liquid helium temperatures. A whole head MEG system (Figure 1b) requires the magnetometer array to be installed in a large dewar which is housed inside a large magnetically shielded room. The typical cost of an MEG instrument is ~$1.5 million and a shielded room is $1.25 million. An additional ~$250,000/year is required to maintain the system. Such costs are a barrier for widespread adoption of MEG as a neuroimaging technique.

In recent years, alkali-metal-vapor atomic magnetometers (AMs) have emerged as a promising non-cryogenic, low-cost alternative to SQUIDs in MEG. AMs can achieve sub-fT sensitivities (Kominis, Kornack et al. 2003) and have been used to detect MEG signals from human subjects (Xia, Baranga et al. 2006). The previous demonstration used bulky vapor cells and free space laser beams to detect MEG signals (Xia, Baranga et al. 2006). It is difficult to envision a free-space laser beam system that could be scaled up into a whole-head sensor array. In contrast, our goal has been to design compact sensors that could realistically be arrayed around the skull. This is a necessary advance toward developing a whole-head MEG system with the full capability of a commercial SQUID-based system.

Because AMs operate near room temperature, a significant portion of the acquisition cost and the bulk of the operating cost is eliminated. Furthermore, the size of the magnetic shield can be dramatically reduced allowing a much smaller system. The use of AMs for MEG offers more

than a simple replacement of current systems. With cost reduced by as much as a factor of 10, one can envision a much broader adoption of MEG as clinical and research tool. For example, the smaller size would enable portable systems deployed in mobile hospitals. The smaller size and cost may also enable improved computer-human interfaces through fast, high fidelity measurements of brain activity.

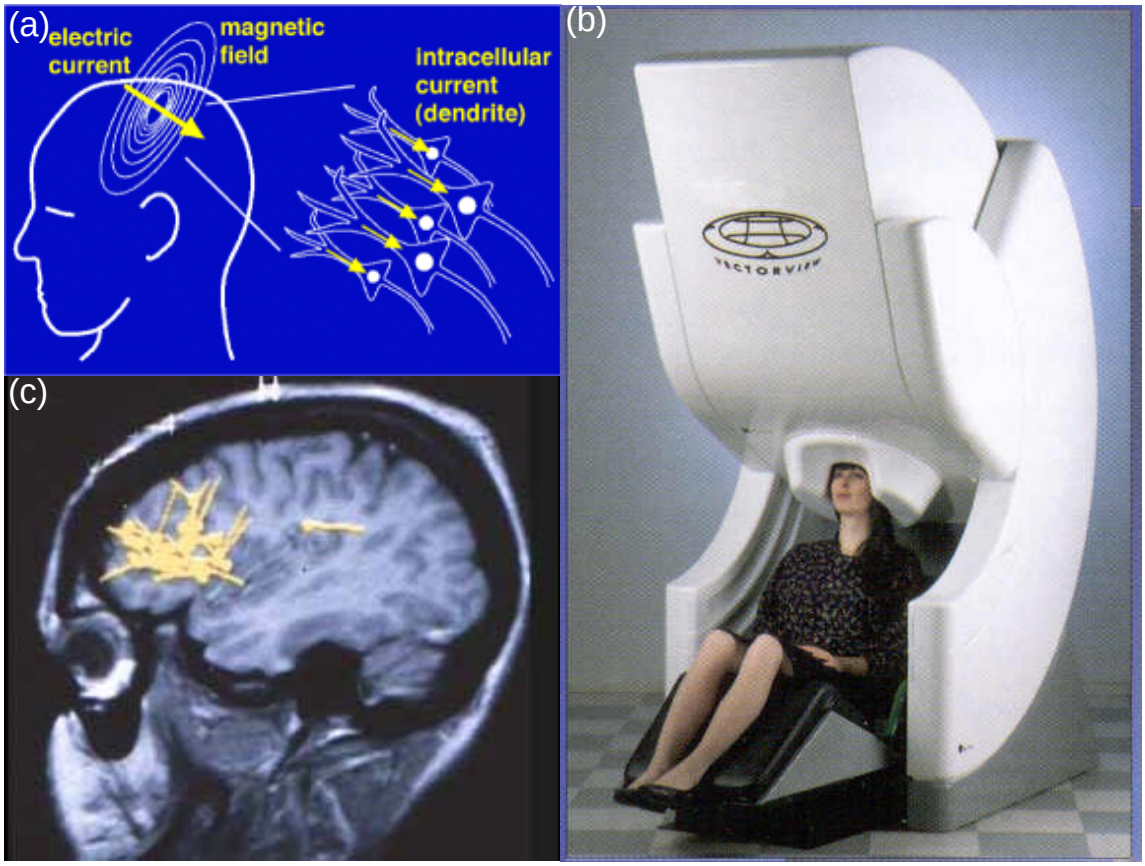

Figure 1: (a) Neural currents produce extremely small magnetic fields (~100 fT at the scalp). (b) Highly sensitive magnetometers arrayed around the head detect these fields with millisecond resolution. The system pictured employs ~300 SQUID sensors that must be cryogenically cooled by 4K liquid helium. (c) Based upon the measured fields, neural currents can be located with sub-centimeter resolution. MEG results (yellow lines) are superimposed on an MRI scan of the brain.

1.2 Atomic Magnetometer Basics

In an AM, the magnetic field is sensed by measuring the interaction between a magnetic field and the electronic spins of a vapor of alkali atoms. The principle of operation for a typical implementation of ultra-high sensitivity atomic magnetometry is shown in Figure 2. A glass cell containing a droplet of alkali metal is heated to produce a high pressure alkali vapor. A circularly polarized "pump" laser beam passes through the cloud of atoms and aligns nearly all of the electron spins along the pump beam optical axis via a process called optical pumping. The

polarization fraction depends on the pump power, detuning, and alkali metal density. A magnetic field perpendicular to the pump beam causes the collective magnetic moment of the atoms to reorient. As a result, the index of refraction of the atomic gas changes. This change in optical properties is measured by detecting the optical rotation of a linearly polarized "probe" laser beam typically oriented perpendicular to the pump beam. Because the measured optical rotation is linear in magnetic field, the output signal acts as a magnetic field discriminator.

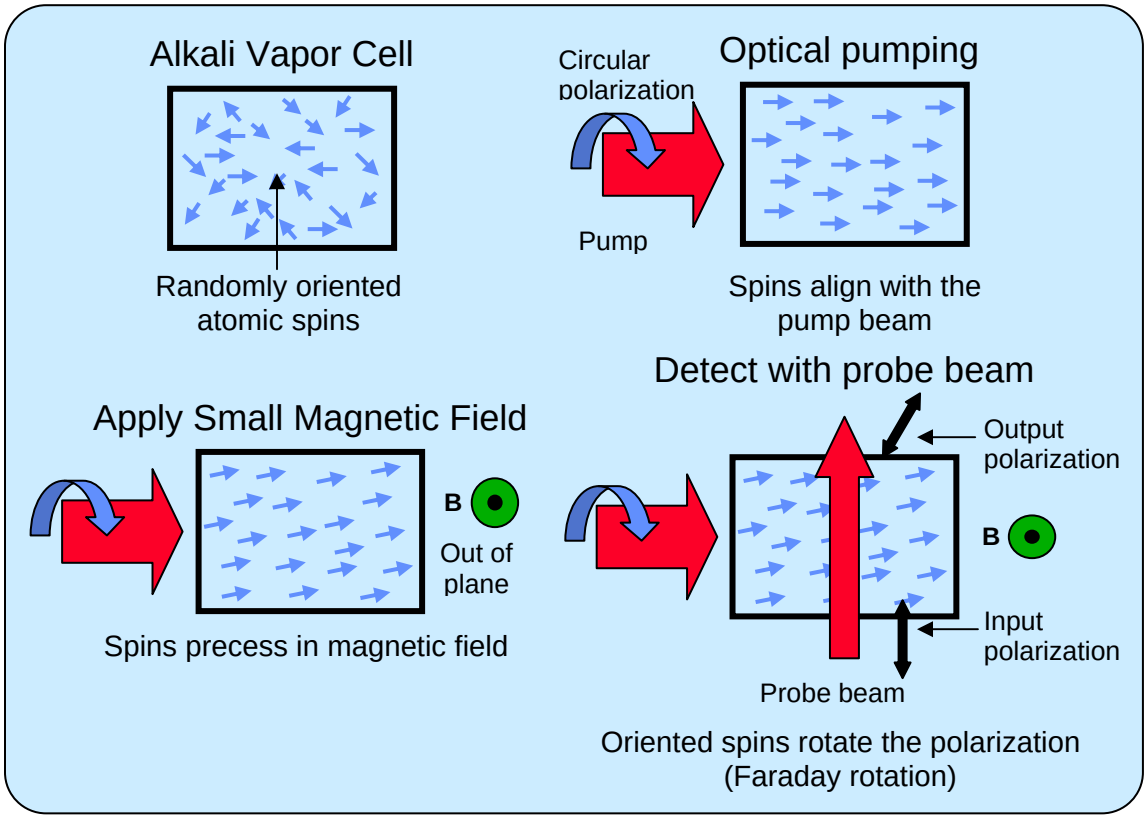

Figure 2: Principle of operation of an atomic magnetometer

The dymamics of the atomic polarization **P**, from which arises the magnetic sensitivity, are described in the equation

$$\frac{d\mathbf{P}}{dt} = D\nabla^2\mathbf{P} + \frac{1}{Q(P)}\left(\gamma\mathbf{P}\times\mathbf{B} + R(\mathbf{s}-\mathbf{P}) - \frac{\mathbf{P}}{T_2}\right).$$

The first term describes diffusion, with diffusion constant D, of the alkali metal atoms through a helium buffer-gas which is typically added to vapor cells at a pressure near atmospheric pressure. The buffer gas slows the polarized atoms' trajectory to the glass vapor cell wall where their polarization is reoriented randomly. The second results in the precession of the polarization with gyromagnetic ratio γ in the presence of a magnetic field **B**. The third term represents the optical pumping at a rate R along the direction of photon spin **s**. The fourth term describes how the optical pumping beam destroys the coherence of **P**. Finally, the fifth term encapsulates all other decoherence processes such as atomic collisions.

The steady state solution of the above equation with a pump beam oriented along z and the only nonzero field equal to Bx is

$$P_z = \frac{R\tau}{\gamma^2 B_x^2 \tau^2 + 1},$$
$$P_y = \frac{\gamma B_x R\tau^2}{\gamma^2 B_x^2 \tau^2 + 1},$$

where $\tau = T_2$. The index of refraction of the atomic gas, assuming a probe beam along the x direction, depends on the atomic polarization as

$$\varphi_{\pm} = \frac{2l\omega}{c}\left(1 + \frac{2\pi n c^2 r_e f}{\omega} D(\omega) \frac{1 \mp P_x}{2}\right)$$

where l is the length of the cell, ω is the frequency of the light, c is the speed of light, n is the number density of the alkali atoms, r_e is the classical electron radius, f is the oscillator strength. The ± refers to right or left circular polarization. For a probe along z, P_x is replaced by P_z in the above expression. The dispersive lineshape function is given by

$$D(\omega) = \frac{\omega - \omega_0}{(\omega - \omega_0)^2 + (\gamma/2)^2}$$

where, ω_0 is the resonant frequency of the optical transition and γ is the width of the optical transition. A rotation of the probe beam's plane of linear polarization arises from the differential change in the index of refraction between its left-handed and right-handed circular polarization components. Because the change in index is proportional to the atomic polarization, the Faraday rotation has a dependence on B_x that is either a dispersive lorentzian (when probed along x) or lorentzian (when probed along z). When probed along x, the linear part of the dispersive lorentzian is used to measure the strength of the magnetic field. When probed along z, phase-sensitive detection is implemented to generate a dispersive lorentzian from the lorentzian profile.

The fundamental sensitivity of an atomic magnetometer operating with density n in a volume V due to shot noise is

$$\delta B = \frac{1}{\gamma\sqrt{nVT_2 t}},$$

where γ is the gyromagnetic ration, t is the measurment time, and T_2 is the transverse decoherence time of the atomic ensemble. Effects contributing to T_2 include collisions with vapor cell walls, optical pumping, and atomic collisions. Spin-exchange collisions are often the largest contribution to the decoherence rate because their cross section is several orders of magnitude larger than the next relevant collisional effect, spin-destruction collisions (Ressler,

Sands et al. 1969; Allred, Lyman et al. 2002). However, by operating in a high density regime where the spin-exchange collision rate is much greater than the Larmor precession frequency it is possible to remove this source of decoherence (Happer and Tang 1973).
Recently, magnetometers operating in this spin-exchange-relaxation-free (SERF) regime have been demonstrated with sensitivities of less than 1 fT/rtHz (Kominis, Kornack et al. 2003; Dang, Maloof et al. 2010). As a result, AMs have begun to impact fields traditionally dominated by SQUIDs, such as biomagnetism, where fields produced by the brain (magnetoencephalography) have been measured (Xia, Baranga et al. 2006). Our work has been primarily motivated by the desire to advance the state-of-the-art in magnetoencephalography (MEG) with AMs by developing compact, scalable, highly sensitive sensors.

2. POTASSIUM FREE-SPACE MAGNETOMETER

Prior to designing and testing the MEG sensor, it was desirable to gain experience and confidence in magnetic sensing below 10 fT/rtHz sensitivity with atomic vapors. In addition, an apparatus suitable for operating and characterizing a sub-10 fT/rtHz sensitivity device did not exist at Sandia. As a result, the first project phase focused on demonstrating sub-10 fT/rtHz sensitivity SERF magnetometry with potassium as had been done in the initial AM-based MEG demonstration.

In the first year, the main goal of the project is to build and characterize a flexible research magnetometer for studying sensor architectures. The overall layout of the magnetometer is shown schematically in Figure 3. The pump beam is passes through the potassium vapor cell polarizing the atoms along the direction of the pump, and the probe beam propagates perpendicularly to the pump. While the pump laser frequency is tuned at or near the potassium D1 resonance to maximize the optical pumping, the probe is linearly polarized and detuned from the D1 resonance to maximize the optical rotation signal. To measure the Faraday rotation signal, the laser beam passes through a photo elastic modulator and a polarizer, aligned orthogonal to the input polarization, before impinging on the photo detector. The photo elastic modulator modulates the polarization by 10°-20° at 50 kHz, and the photo detector signal is demodulated by a lock-in amplifier. With this configuration as a magnetic field perpendicular to the plane of the pump and probe beam is swept, the output of the lock-in amplifier is a dispersive Lorentzian. DFB (distribute feedback) lasers were chosen for their relatively high power of 80 mW although more power may be required for the laser that optically pumps the atoms when more than a few channels are needed. To gain spatial information about how the magnetic field varies across the vapor cell, we detect the probe beam with a 2 × 3 array of photodiodes; the signal on each photodiode corresponds to the magnetic field in spatially separated regions of the vapor cell. Signals can then be subtracted to obtain the magnetic field gradient and reduce common mode noise.

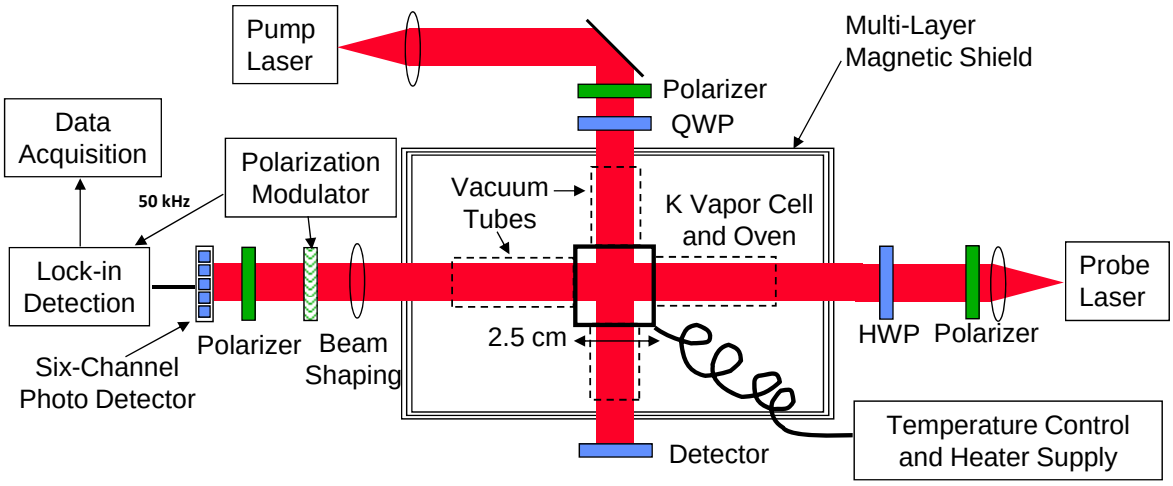

Figure 3: Schematic of potassium research magnetometer.

The magnetic shield is a four-layer nested-cylinder design fabricated from a high permeability alloy (Figure 4). With four layers, the expected shielding factor (the ratio of the external field to the internal field) is ~10^6, although this was never experimentally measured. The size of the internal shield was chosen to balance the improved shielding with smaller size and the reduced intrinsic magnetic field noise from the magnetic shield with larger size. With an interior diameter of 8 inches the estimated magnetic field noise is 9 fT/Hz$^{1/2}$, which is further reduced by a factor of ~10 when the device is operated as a gradiometer. This will allow us to demonstrate a magnetometer with a sensitivity of < 10 fT/Hz$^{1/2}$. As seen in our measurements below, the magnetic field noise produced by the shield was ~15 fT/Hz$^{1/2}$. A coil system allows three-axis control of the interior magnetic field. The longitudinal field is produced by a solenoid wound around an acrylic tube (see Figure 5). The solenoid windings are spaced by 0.8 inches. Fields transverse to the longitudinal axis of the solenoid are produced by wrapping two "cosine coils" around the tube. The cosine coils are printed on a large Kapton flexible circuit board that has dimensions equal to the length and the circumference of the acrylic tube.

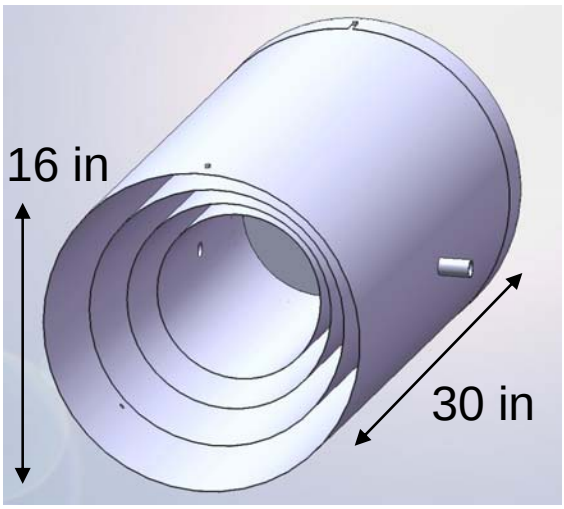

Figure 4. Drawing of the four-layer magnetic shield.

The shield contains the atomic vapor cell within an oven, and coils to control the field in all three axes. One of the major concerns entering the project was where to procure a high buffer gas pressure vapor cell. Fortunately, we were able to purchase one commercially from Technical Glass in Colorado. The vapor cell is placed inside of an oven (Fig. 3) to heat the vapor cell to 150-180 ºC with resistive heater elements. The elements are constructed by twisting a fine gauge wire (36 or 32 AWG) that is insulated with a high temperature coating. The oven is constructed from boron nitride and is insulated with an aerogel blanket insulation. We use both a

nickel/chrome alloy insulated with polyimide and a titanium wire insulated with a ceramic. The nickel/chrome wire was much easier to work with because it was solderable and robust to multiple bending of the wire, but its temperature was limited by the polyimide. The titanium could go to higher temperature, but was prone to failure because the electrical connections to the heater were formed by twisting the titanium wire around copper leads and the ceramic insulation breaking forming electrical shorts. The laser beams pass through evacuated tubes that provide both insulation for the oven and prevent the beams from passing though disturbed air from the high temperature gradients.

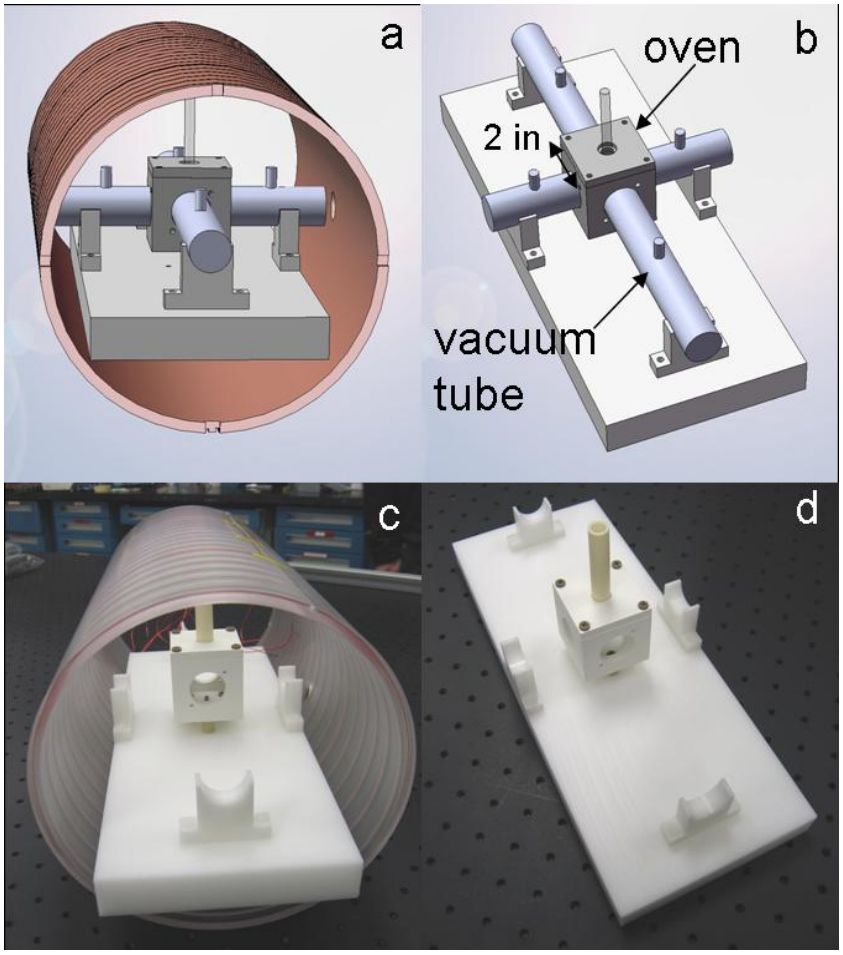

Figure 5. A drawing (a) and a photo (c) of the coil form and oven which is inserted inside the shield. A drawing (b) and a photo (d) of the oven for the potassium vapor cell. The drawing shows the vacuum tubes through which the lasers propagate.

The performance of the magnetometer is shown in Figure 6. The frequency response of the magnetometer is determined by applying a chirped sine wave to the magnetic field along the sensitive axis of the magnetometer. The magnetometer has a 3 dB bandwidth of 5 Hz. For MEG a bandwidth of 50 Hz would be preferable. The measured output rms voltage noise converted to units of magnetic field and divided by the normalized frequency response is shown in Figure 4. The sensitivity of a single channel is 15 $fT/Hz^{1/2}$ over a frequency range of 5 to 40 Hz, which we attribute to the magnetic field noise produced by the magnetic shield. If we subtract two adjacent channels the magnetic field noise can be reduced by nearly a factor of four revealing the intrinsic sensitivity of the individual channels. Between 10 and 20 Hz the intrinsic sensitivity is 4 $fT/Hz^{1/2}$. Figure 7 shows the noise from the photodetectors under three different conditions: the noise when the magnetometer is operational, the optical noise when the pump beam is blocked, essentially turning off sensitivity to magnetic fields, and electronic noise when no light is on the detector. When the magnetometer is operational, there is significant $1/f$ noise below 20 Hz, and the optical noise does not contribute significantly to the $1/f$ component. This noise seems to be either magnetic in origin or is associated with the pump laser beam. We did not determine the origin of this noise. At frequencies above 20 Hz the system is dominated by optical probe beam noise.

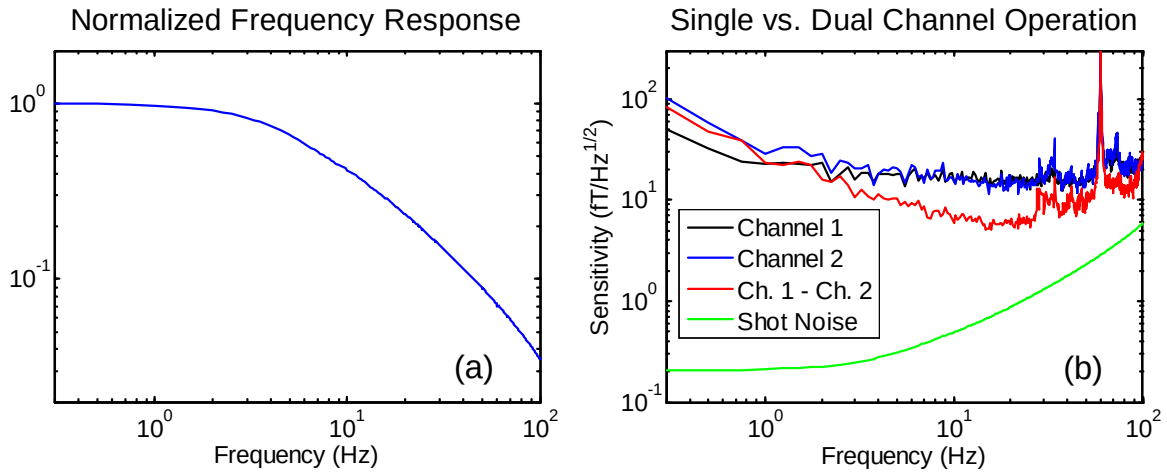

Figure 6: Potassium magnetometer normalized frequency response (a) and sensitivity (b) as a function of frequency. The sensitivity plot shows how subtracting two channels can eliminate common mode noise to show the intrinsic sensitivity of each channel. Note that the red trace should be divided by a factor of $2^{1/2}$ to indicate the noise of a single channel. The green line is the photon shot noise limit of the magnetometer.

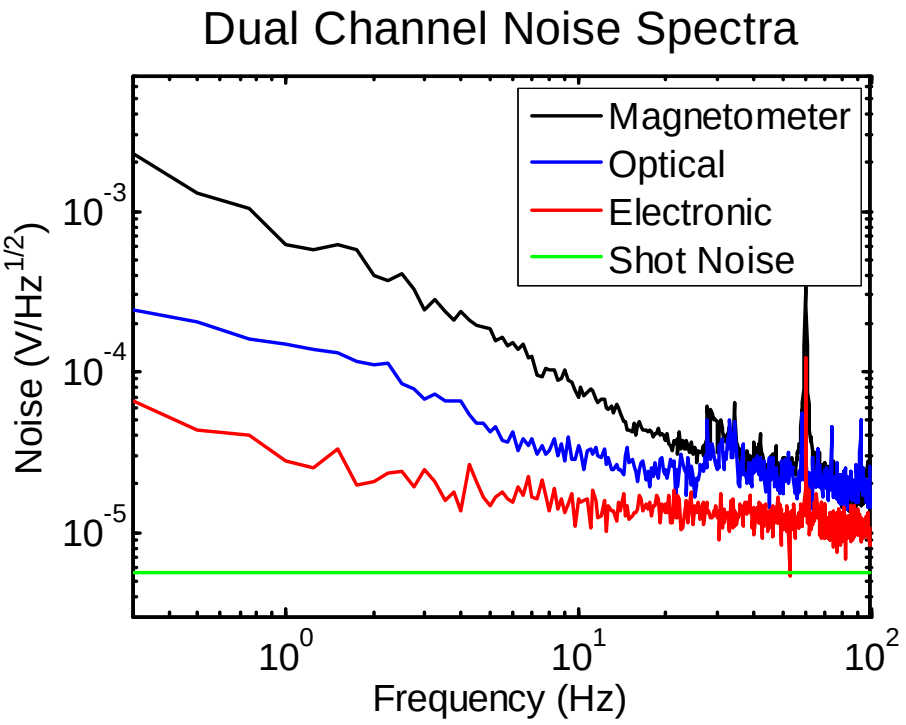

Figure 7: Noise spectra from two subtracted photodiodes.

3. RUBIDIUM FIBER-COUPLED MAGNETOMETER DESIGN/TESTING

The most common SERF AM implementations are similar to that described in the previous section with free-space pump and probe beams oriented orthogonally and both beams tuned near the D1 transition. This geometry allows independent manipulation of the pump and probe beams for magnetometer optimization and was used in the previous demonstration of AM MEG (Xia, Baranga et al. 2006). While the proof-of-principle AM MEG measurement was groundbreaking, it is difficult to envision a whole-head MEG system using free-space beams and large vapor cells. If noncryogenic AMs are to replace SQUIDs in MEG, it is crucial to develop sufficiently sensitive AMs that can be conveniently arrayed around the scalp.

In order to develop AMs that can be densely packed into a whole-head array, several design criteria are critical. Free-space beams must be eliminated in favor of fiber-optic light delivery to individual vapor cells. This has been successfully implemented in an array of magnetometers used for magnetocardiography (Belfi, Bevilacqua et al. 2007; Bison, Castagna et al. 2009; Knappe, Sander et al. 2010). However, the fields produced by the heart (~ 100 pT) are approximately three orders of magnitude larger than those produced by the brain (~ 100 fT), so it is necessary to maintain the sub-10 fT/rtHz sensitivity of the original MEG demonstration (Xia, Baranga et al. 2006). In addition, the footprint of the AM on the head must closely match the 30 mm X 30 mm dimension of the SQUID MEG sensors to enable dense arraying. Also, the distance between the sensing volume and the head must be as small as possible to maximize the detected signals from the brain. Finally, a simple optical design will benefit the long-term stability and ease of operation of an AM-based MEG array.

3.1 Two-color pump probe magnetometer design

Designing a fiber-coupled AM with a small footprint on the head becomes simpler if the crossed pump/probe beam geometry is abandoned in favor of a single optical axis shared by both beams. A single-axis SERF magnetometer has been demonstrated using a single elliptically polarized beam in which the circular component of the beam provides the pumping source while the linear component serves as probe (Shah and Romalis 2009). Because the pump/probe are parallel, P_z is probed in the polarization analyzer. A signal proportional to B_x is generated by introducing a uniform sinusoidal magnetic field modulation along the x axis in the region of the atomic vapor cell and performing lock-in detection of the polarization analyzer output signal (see Eq. (10) of (Shah and Romalis 2009). Lock-in detection also improves sensitivity by moving the measured signal away from low-frequency noise associated with laser beam jitter. The magnetometer is sensitive to the magnetic field component parallel to the applied modulation. As a result, it is possible to probe any field component perpendicular to the optical axis without adjusting any optics by applying the modulation along the desired sensitivity axis. This is an important advantage over the orthogonal-beam design. This elegant, compact implementation achieved a sensitivity of 7 fT/rtHz (Shah and Romalis 2009). However, because a single beam is used, pump and probe parameters cannot be independently tuned for straightforward magnetometer optimization.

We have developed a magnetometry scheme that combines the simplicity of a single optical axis with the convenience of independent pump/probe parameter adjustment. This is made possible

by overlapping pump and probe beams that operate at different wavelengths. The AM implementations discussed above perform both the pumping and the probing near the D1 line. However, it is also possible to probe on the D2 line. For rubidium, the D1 (795 nm) and D2 (780 nm) lines are sufficiently far apart that the beams can be manipulated with dichroic optics. Assuming linearly polarized input light, a multiorder waveplate can be designed to introduce a quarter-wave delay at 795 nm and a half-wave delay at 780 nm. At the waveplate output the 795 nm light is circularly polarized to provide optical pumping while the 780 nm light remains linearly polarized for detection of Faraday rotation. After both beams have interacted with the atomic vapor, the pump beam can be filtered out with an interference bandpass filter centered at 780 nm to eliminate extraneous light levels from entering the polarization analyzer.

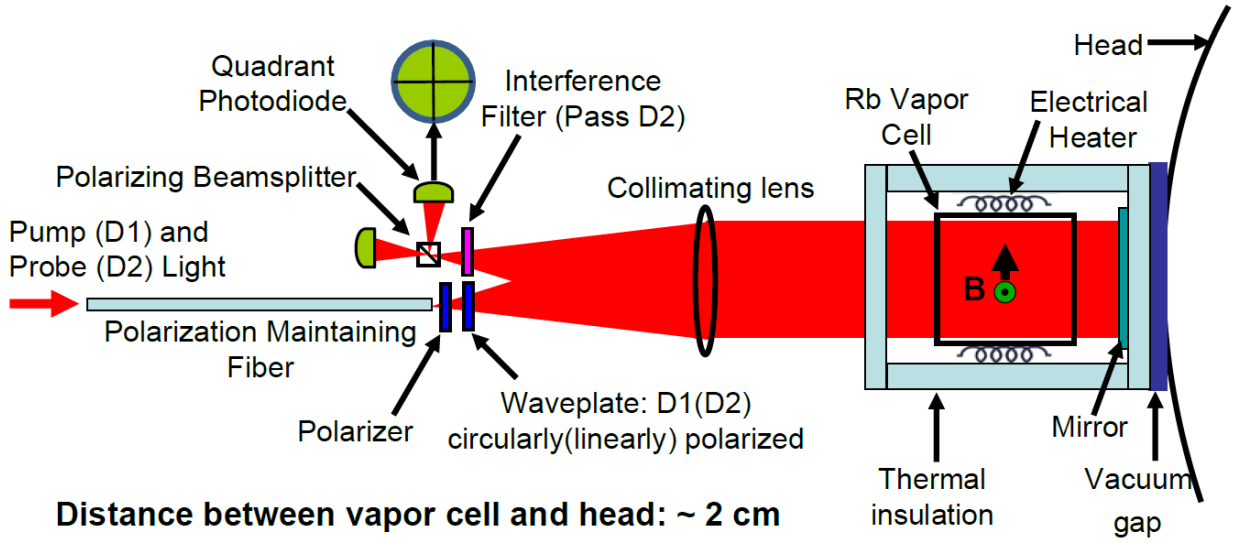

Figure 8: Schematic of Sandia MEG magnetometer design

Based upon the two-color pump/probe scheme, we have designed a compact, fiber-coupled magnetometer tailored to the MEG application. A schematic of the design is shown in Figure 8. Distributed feedback lasers at 795 nm and 780 nm are coupled into the same polarization maintaining (PM) optical fiber using a PM fiber combiner. At the fiber output, a polarizer cleans up the pump/probe polarization. The beams next pass through a multiorder quartz waveplate that has wavelength-dependent birefringent indices of refraction. Waveplate thickness is chosen to introduce a quarter-wave delay to the pump beam and a half-wave delay to the probe beam. Specifically, the thickness is 1.09 mm, resulting in 12.5 waves at 780 nm and 12.249 waves at 795 nm. At the waveplate output, the pump light is circularly polarized while the probe remains linearly polarized.

After passing through the polarization optics, the beams are collimated and pass through a cylindrical glass vapor cell containing a small droplet of ^{87}Rb metal. The decoherence rate due to collisions with the uncoated vapor cell walls is minimized by an atmosphere of helium buffer gas in the cell, resulting in a long diffusion lifetime. Nitrogen is also added to the cell at a pressure of 30 Torr to assist in the optical pumping process by quenching the excited state. The cell dimensions (25 mm diameter, 25 mm long) were chosen to closely match the size of SQUID MEG sensors. The cell is housed within a microporous ceramic oven to provide thermal

isolation. The cell is heated to ~ 190 Celsius with an AC-electrical signal at 20 kHz, implying a rubidium density of 6 x 10^{14} per cm^3.

Because we desire to perform MEG measurements, it is advantageous to place the vapor cell as close to the head as possible. To this end, we place a retroreflecting mirror in the optical path after the vapor cell, reflect the beam back through the vapor cell, and focus it onto a polarization analyzer located away from the head. Immediately before entering the polarization analyzer, the D1 pump light is filtered out by an interference bandpass filter centered at 780 nm. The polarization analyzer consists of a polarizing beamsplitter and a quadrant photodiode (QPD) in each beamsplitter output arm. Due to the requirement that no magnetic materials could be used in the sensor, it was necessary to have a custom gold-on-quartz package fabricated for the quadrant photodetectors. The probe beam is centered on the QPDs through a combination of adjustments of the collimating lens and the QPD locations, resulting in each quadrant detecting the signal from a different part of the vapor cell. Photodiode currents from the same quadrant in each arm are subtracted, resulting in four output channels that measure the magnetic field in different quadrants of the atomic cloud.

Although the polarization of each beam cannot be independently manipulated in our design, adjusting the waveplate angle to appropriately prepare our beam polarizations has always been straightforward. The power and detuning of both lasers are manipulated independently to optimize the magnetometry signal.

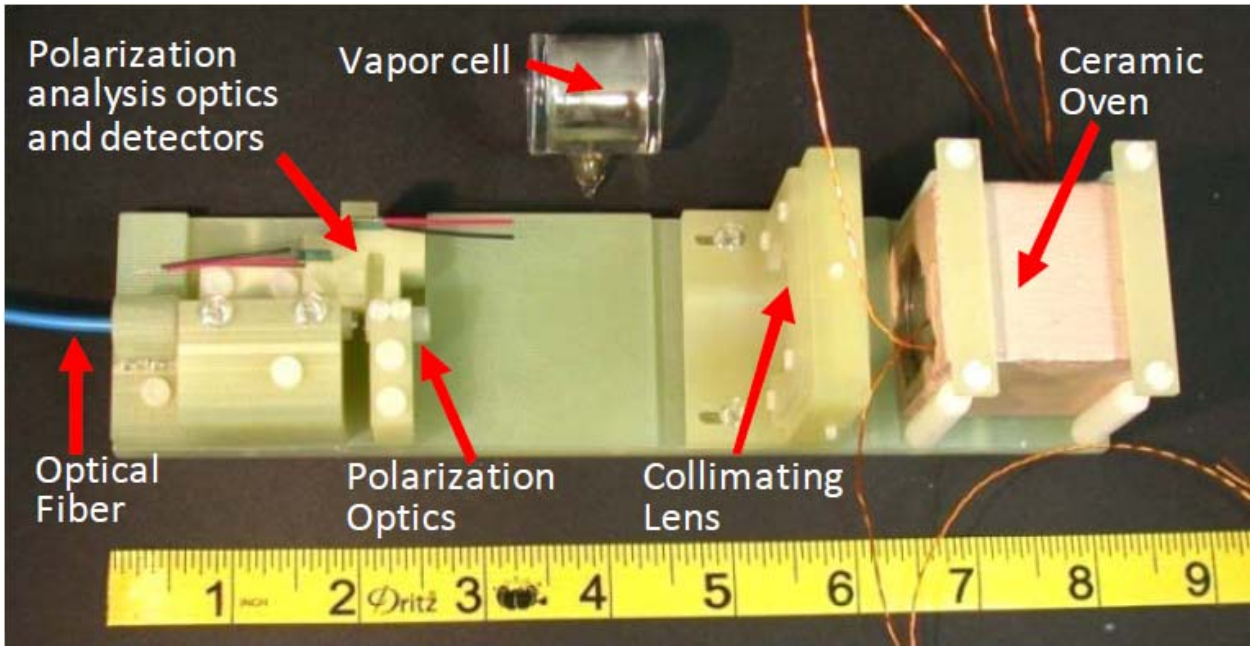

Figure 9: Photograph of the assembled magnetometer and a rubidium vapor cell. Tape measure units are inches. The optical mounts and mechanical support structure are machined from G-10 garolite fiberglass-epoxy composite.

Figure 9 shows a photograph of the assembled magnetometer hardware. A vapor cell is shown alongside the magnetometer. All of the materials are nonmagnetic, with the bulk of the optics

mounts and mechanical structure being machined from G-10 garolite fiberglass-epoxy composite. Although in this photograph the polarization analyzer has single element photodetectors, the measurements presented were taken using quadrant photodetectors. Much of the length of the magnetometer is necessary to allow the fiber output to freely expand until achieves the diameter of the vapor cell. This length could be reduced substantially by introducing a telephoto lens arrangement between the polarization optics and the vapor cell.

3.2 Sensitivity Measurements

Magnetic sensitivity measurements are performed inside the magnetic shields described in Section 2. We select an axis of sensitivity by introducing a 1 kHz magnetic field modulation perpendicular to the optical axis and performing lock-in detection on the polarization analyzer output signals. Details of this technique are found in (Shah and Romalis 2009). The resulting signal is a dispersive lorentzian curve centered at zero magnetic field. Field measurements are taken by zeroing the ambient magnetic fields such that we are centered on the linear portion of the dispersive lorentzian. Sensitivity (δB) is determined by measuring the noise spectrum (S_{noise}) of the magnetometer output and dividing it by the slope (dS/dB) of the magnetic resonance ($\delta B = S_{noise}/\{dS/dB\}$). The magnetometer bandwidth is measured by introducing a swept-sine magnetic field to the atomic ensemble and measuring the frequency response on an FFT analyser.

Figure 10 shows a plot of measured sensitivities that have been normalized to the measured bandwidth of 20 Hz. The blue curve shows the sensitivity of a single channel of the quadrant photodiode output. The ~ 15 fT/rtHz observed between 3--40 Hz is consistent with the expected noise floor of the magnetic shields and similar to what we observed with the potassium SERF magnetometer installed in the same set of shields. Above 40 Hz, sensitivity is near the shot noise limit, but there appears to be some additional technical noise from our probe laser (shown in magenta). Because the output signals from the quadrant photodetectors are measurements of the magnetic field in different regions of the cell, it is possible to measure gradients in the cell by subtracting these signals in various combinations (see Figure 11). The green and red curves in Figure 10 are the noise spectra for the horizontal and vertical gradients that result from these subtractions. Because gradient signals remove magnetic noise common to all channels, they represent the intrinsic sensitivity of a single channel output. The resulting intrinsic single channel sensitivity is < 5 \fthz between 5--10 Hz, remains < 10 fT/rtHz down to 1 Hz, and is shot noise limited above 10 Hz.

Although the measured sensitivites are adequate for MEG and comparable to previous AM implementations, we have not exhaustively searched for the best operating point of our two-color magnetometer. In the near future we plan to explore the parameter space more completely in both simulation and experiment and anticipate an improvement in magnetometer bandwidth while maintaining current sensitivity. In particular, we anticipate that the bandwidth can be improved by operating the vapor cell at higher temperature (i.e. higher density) thereby increasing the spin destruction collision rate (Shah and Romalis 2009). This requires adapting our optical design because we cannot increase the temperature further without damaging the dielectric mirror attached to the vapor cell. Details of the sensor design and performance were presented at the IEEE 2010 International Frequency Control Symposium and are available in the conference proceedings (Johnson and Schwindt 2010).

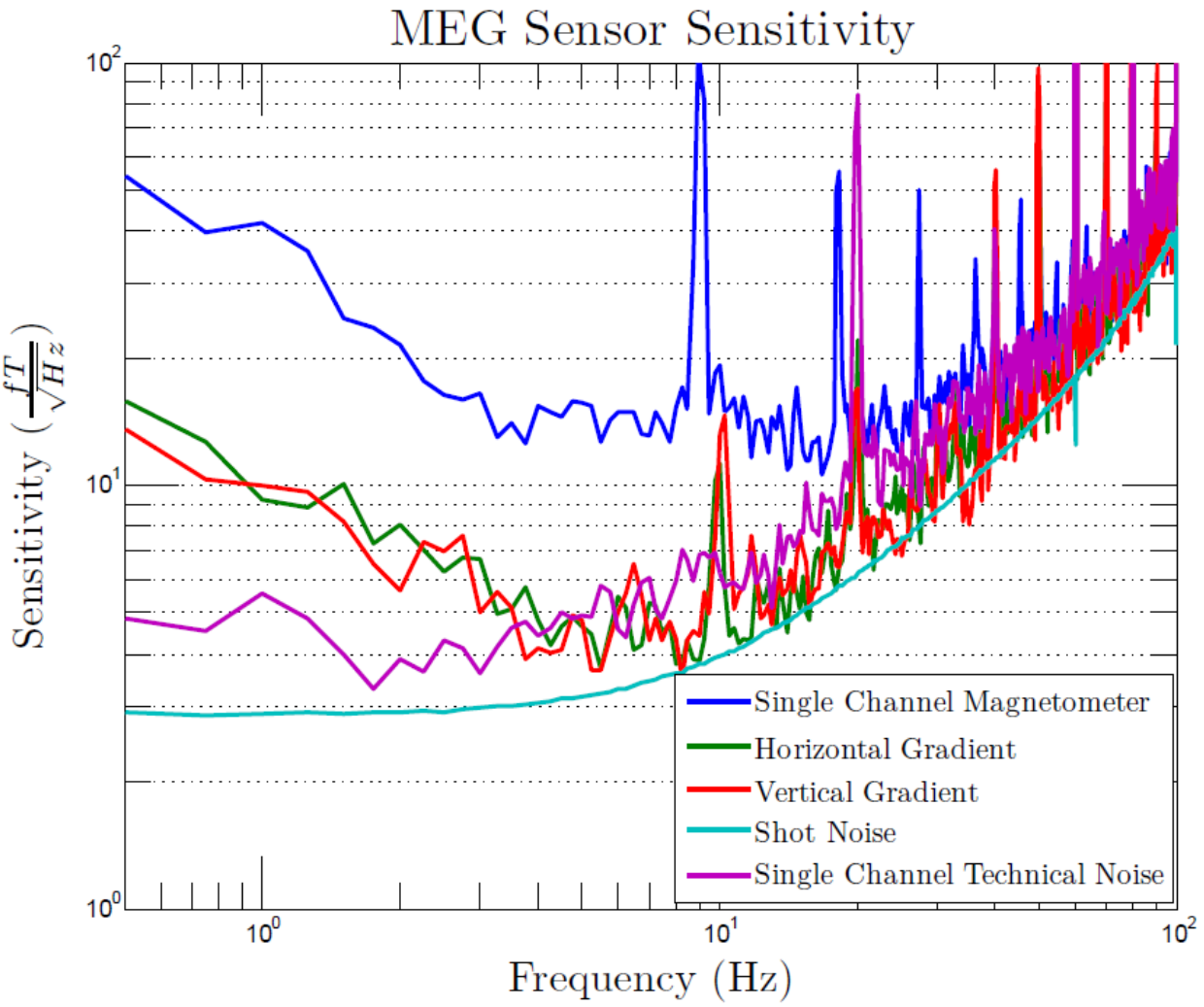

Figure 10: MEG sensor sensitivity between 5-100 Hz.

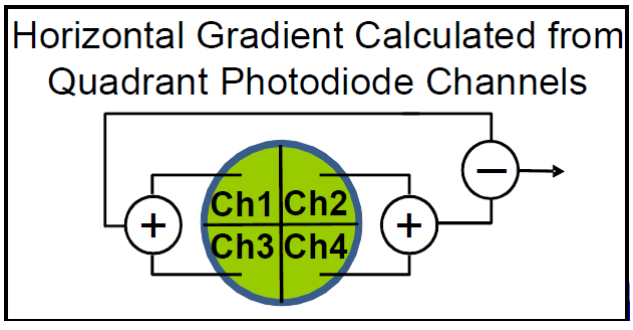

Figure 11: Calculating the horizontal gradient from the quadrant photodiode signals.

3.3 Protection of Human Subjects

The safety and comfort of the human subject must be ensured. Per federal regulation, the Sandia Human Studies Board extensively reviewed the proposed human studies and compiled a list of recommendations. Foremost among their requirements was to ensure there would be sufficient thermal isolation between the 200 Celsius vapor cell and the scalp. The microporous ceramic oven that houses the cell provides the first layer of thermal isolation, resulting in a 90 Celsius temperature on the outside surface of the oven. A custom G-10 garolite fiberglass-epoxy composite vacuum vessel provides the final layer of thermal isolation. The magnetometer fits tightly inside the vacuum vessel to keep the vapor cell ~ 1 cm from the scalp. The surface of the evacuated vacuum vessel remains within a few degrees Celsius of internal body temperature when the vapor cell is held at 200 Celsius. Figure 12 shows a photograph of the MEG magnetometer installed inside the vacuum vessel. The optical fiber, vapor cell heater/temperature sensor wiring, and quadrant photodiode signals pass through the vacuum vessel on vacuum feedthroughs. The nonmagnetic vacuum valve is made of glass with a Teflon stem and rubber sealing o-ring. The vacuum vessel footprint on the head is 60 mm X 60 mm.

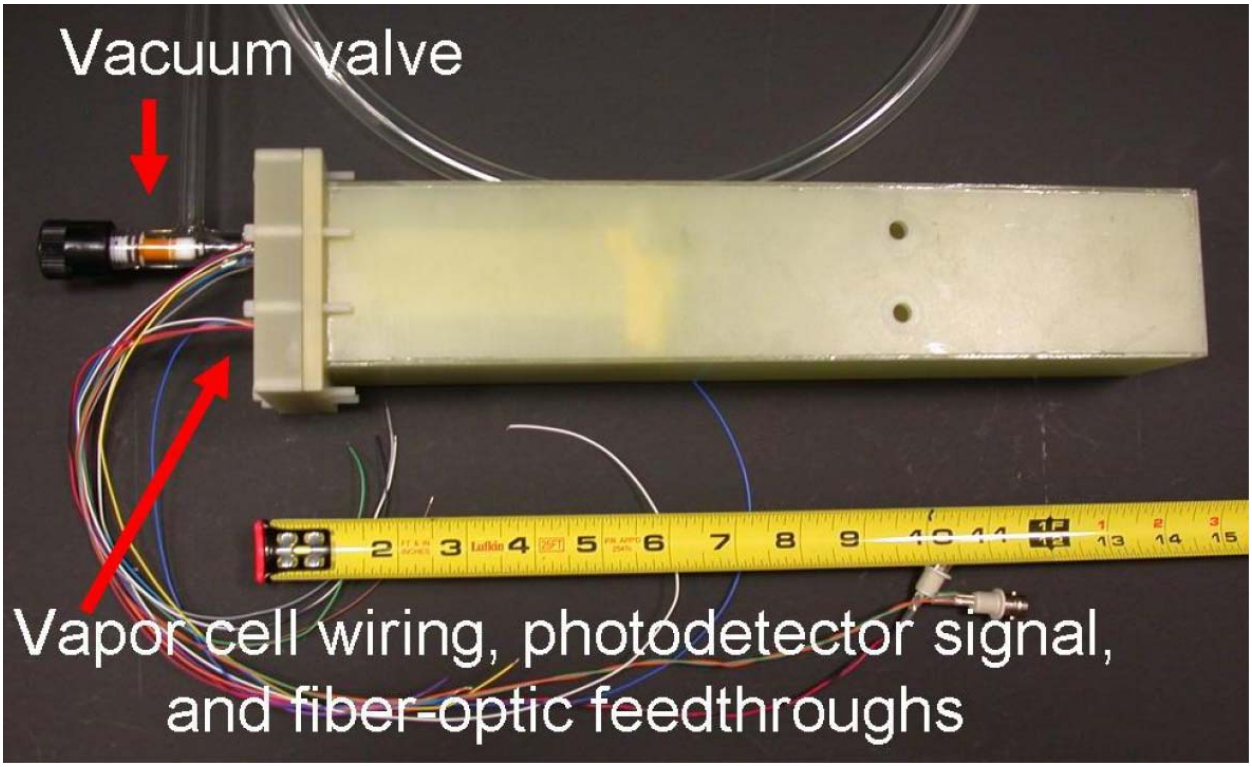

Figure 12: Photograph of the magnetometer mounted inside the vacuum vessel. Tape measure units are inches. The length of the vacuum vessel provides excess interior space for routing of the fiber optic cable and electrical wires and could be substantially reduced. The holes visible on the top surface of the vacuum vessel assist in assembly and are sealed prior to evacuation.

4. HUMAN SUBJECTS MEASUREMENTS

The two-color pump/probe magnetometer satisfies nearly all of the criteria listed above for a viable MEG magnetometer: fiber coupling, sub-10 fT/rtHz sensitivity, small distance between the scalp and the sensing volume, and a simple optics package. Although the footprint of our current design is approximately 50 mm X 50 mm, the vapor cell is adequately small and miniaturization to the SQUID dimensions should be straightforward. In addition to the lab demonstration of MEG-compatible sensitivity, several other factors must be addressed before performing MEG on human subjects.

4.1 Experimental Setup at The Mind Research Network

A suitable zero-field environment large enough for a human subject must be arranged. Through a collaboration with The Mind Research Network (MRN) on the University of New Mexico campus, we have access to a large magnetically shielded room that houses a SQUID-based MEG system. The two-layer μ-metal room has a shielding factor of ~ 1000, resulting in an ambient field of tens of nanotesla. Because our magnetic resonance width is typically < 5 nT, this is insufficient. In order to zero the remaining field, we have designed a system of 18 coils wrapped on the outside of a 1.16 m diameter, 1.22 m length cylinder (see Figure 13). The sensor is installed near the center of the system of coils. The cylinder is sufficiently large to comfortably fit the head and torso of a human subject. The coils are connected to 18 computer-controlled current supplies. The field **B** produced by the coils is **B = M I**, where **I** is a vector of the currents in each coil and **M** is the matrix of current-to-field conversion factors. **M** is measured by activating each coil individually and recording with a fluxgate magnetometer the field produced in the region of the MEG sensor. Prior to beginning MEG measurements, the ambient field is measured, and the combination of currents needed to create a zero-field environment is calculated by simple linear algebra. DC currents are output to the custom-designed coils via a Labview program. The supplies have a modulation input, so by appropriately modulating the currents supplied to the coils, field modulations can be introduced to select a sensitive axis via lock-in detection.

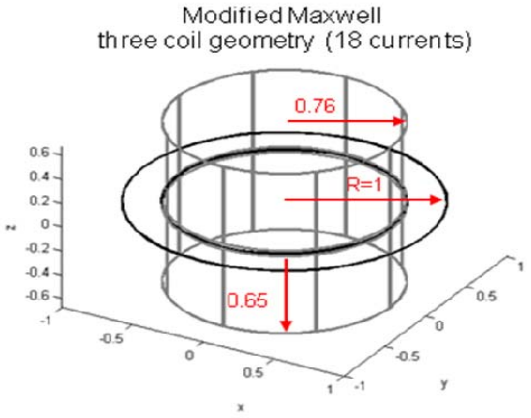

Figure 13: Geometry of the 18 coil system. There are 16 square-shaped coils wrapped on the surface of cylinder, one circular coil wrapped around the center of the cylinder, and another circular coil spaced outside of the main cylinder. Listed dimensions are relative to radius of the large coil.

A human subject lays on a platform integrated with the coil system and rests their head against the sensor as MEG measurements are taken. Figure 14 shows a human subject preparing for MEG measurements inside the coil system.

18-coil field cancellation system for reducing the field from ~100 nT to < 1 nT

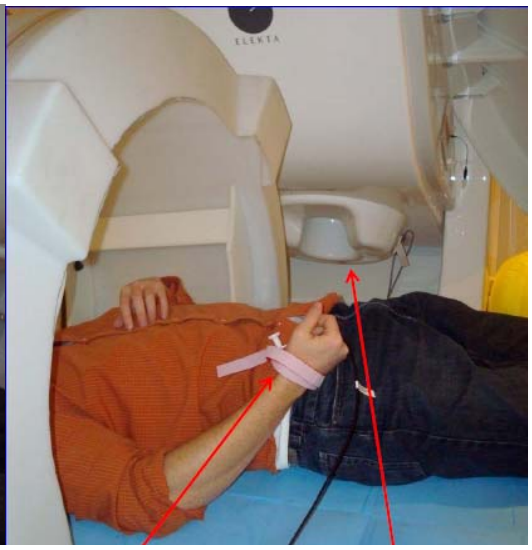

Median nerve stimulator

SQUID MEG system

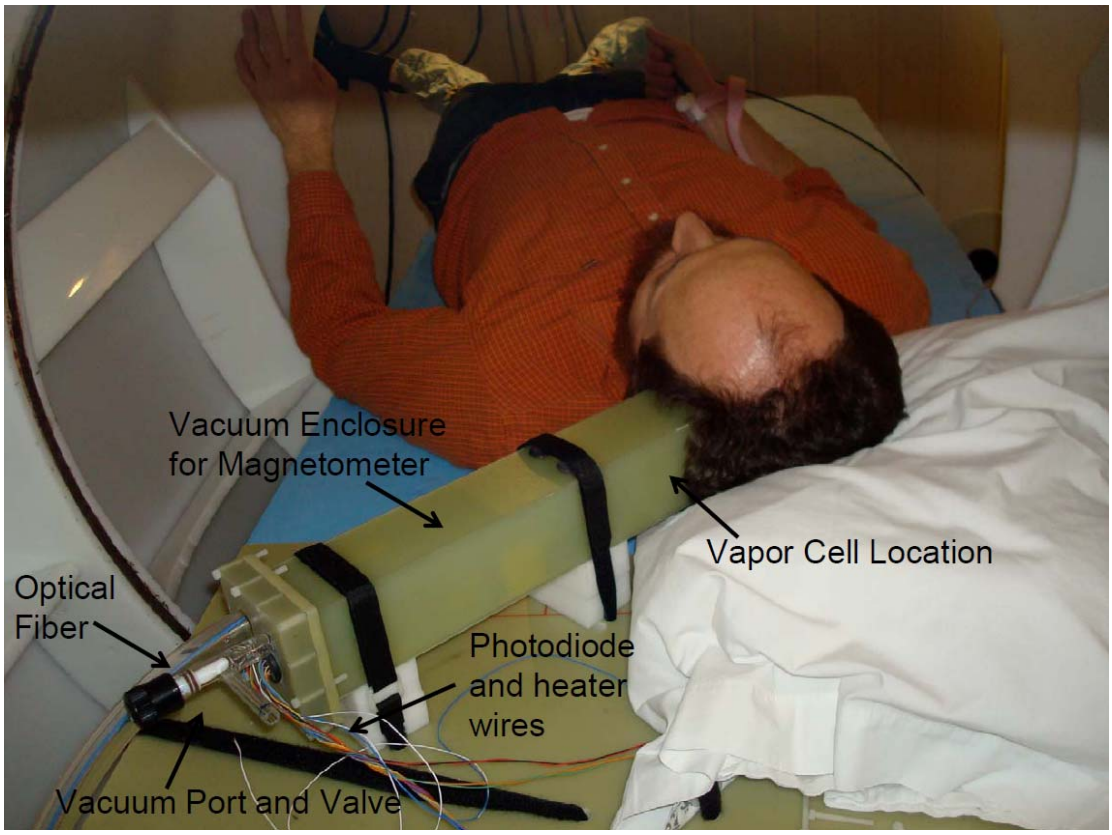

Figure 14: Human subject preparing for MEG measurements at The Mind Research Network.

Because MEG measurements are made at MRN, which is located seven miles from Sandia National Laboratories, our entire magnetometry system must be portable. We have installed all lasers, optics, data acquisition, and peripheral electronics on a rolling cart for ease of transport to MRN. Over the course of a single afternoon, the entire system can be moved from Sandia to MRN and fully assembled to begin making MEG measurements. The MRN facility houses a commercial SQUID-based MEG system manufactured by Elekta (Elekta Neuromag: http://www.elekta.com). This allows both SQUID and AM MEG measurements to be taken in an identical environment.

4.2 Single Sensor MEG measurements

Our initial MEG studies were performed on a single adult male using a single AM sensor and the Elekta SQUID system. Before presenting the results, it is instructive to contrast the signals obtained from the two sensor types. The atomic magnetometer is sensitive only to magnetic fields perpendicular to the optical axis. Because the optical axis is perpendicular to the scalp, only fields tangential to the scalp can be detected. In contrast, the SQUID sensors are pick-up coils oriented in a plane tangential to the scalp. Therefore, the SQUIDs are sensitive to fields perpendicular to the surface of the head. Figure 15 illustrates the difference between the detected field components. Because the sensors detect different field components, we can only test to see if the AM reproduces the temporal field profile detected by the SQUIDs but cannot make absolute comparison of signal amplitudes.

Two measurement modalities were used: median nerve stimulation and auditory stimuli. Median nerve stimulation is performed by placing electrodes on the wrist and delivering a harmless current pulse. Auditory stimuli consists of a series of irregularly spaced tones delivered by headphone to the subject's ear. The evoked responses from both median nerve and auditory stimulation were recorded at 1 kHz on one adult male test subject using the AM and the Elekta-Neuromag SQUID-based MEG system. The right median nerve was electrically stimulated with square pulses 200 μs wide and 8 mA in amplitude at intervals varying between 700 ms and 1200 ms while recording the signals on the left side of the head near the somatosensory cortex. The interval between stimuli presentation was varied randomly to prevent subject adaptation. Data was filtered with a 1--150 Hz bandpass filter and a 60 Hz notch filter with a 5 Hz width. Auditory stimuli consisted of 250 ms 1000 Hz tones presented to both ears while the AM was placed over the auditory cortex on the left side of the head. The interval between tones was chosen at random to be either 900 ms, 1000 ms, or 1100 ms. Auditory responses were filtered with a 1--40 Hz bandpass filter. Figure 16 shows the signals from the AM and four SQUID channels in a similar location. The sensitive axis of the AM was tangential to the scalp along a line drawn from the ear to the top of the head. Because the SQUIDs detect the field component

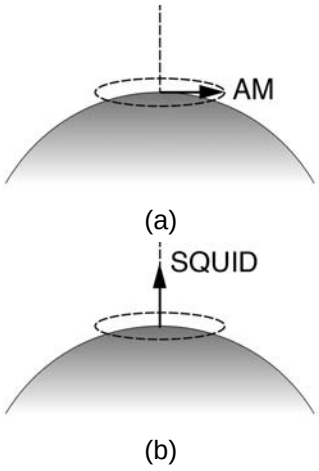

Figure 15: Field orientations measured by an atomic magnetometer [AM, Part (a)] and a SQUID sensor [Part (b)].

perpendicular to the head, it is reasonable that the detected signals are not identical. However, the temporal profiles in the first 100 ms are comparable, indicating that the AM bandwidth and sensitivity is sufficient to perform MEG measurements in the auditory and somatosensory modalities, although increasing the bandwidth should remain a future research goal. The AM channel noise is more highly correlated than the SQUID channels because the AM baseline (5 mm) is much smaller than the SQUID channel separation (~ 30 mm).

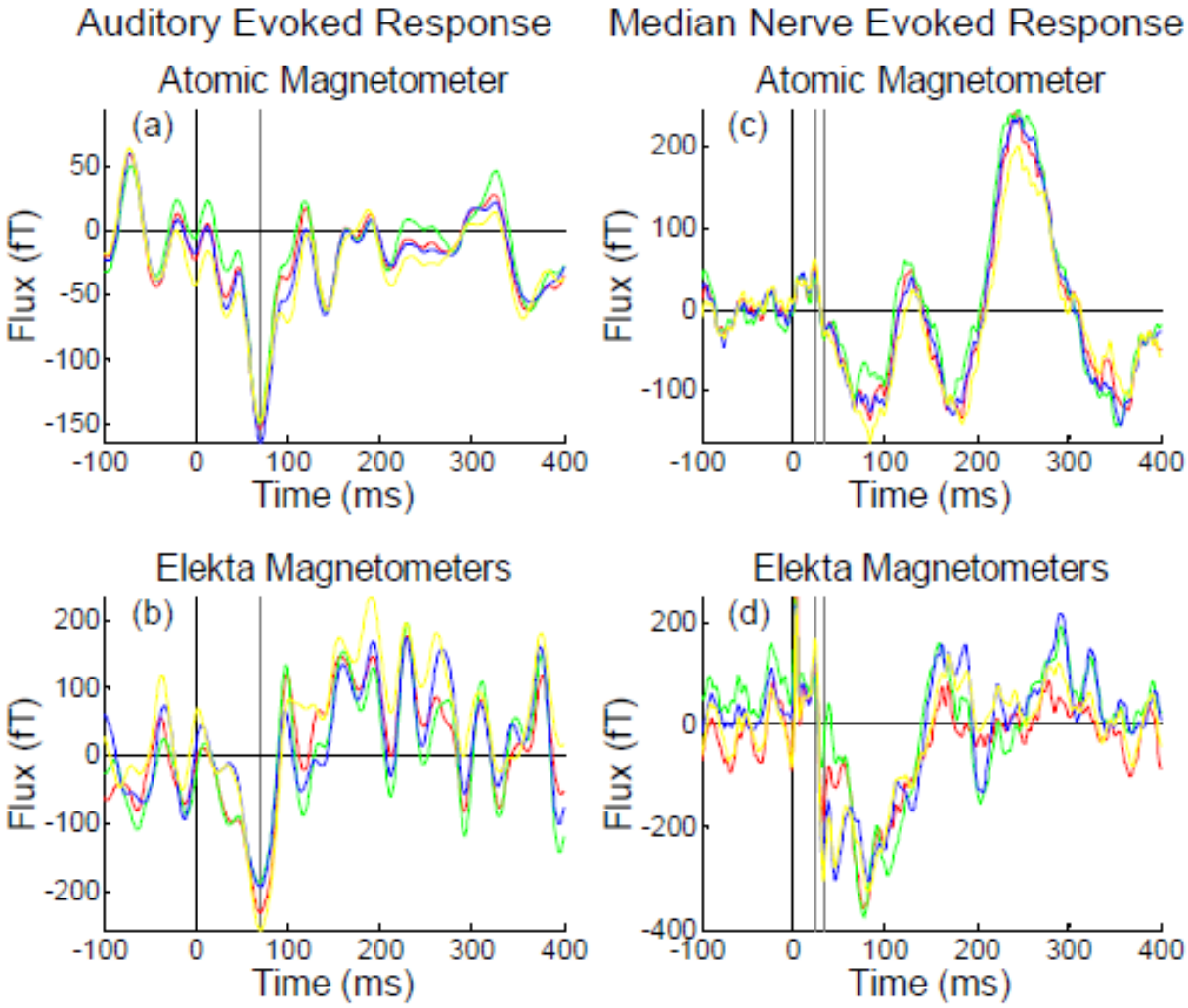

Figure 16: MEG signals recorded by the four-channel atomic magnetometer (AM) and four Elekta SQUID magnetometers located near the AM position. Plot a(b) shows the average evoked response from 320(110) auditory stimuli for the AM(SQUIDs). Plot c(d) shows the average evoked response from 368(313) median nerve stimuli for the AM(SQUIDs). Stimuli were applied at t = 0 s. Grey vertical lines indicate important evoked responses commonly used in MEG studies. Because the sensors measure different field components, the signal strength is not expected to be identical. However, the temporal profiles are comparable.

Our initial single-sensor results represent a world-first in performing MEG with a non-cryogenic sensor that has potential to be densely arrayed around the head for in a whole-head MEG system and have been accepted for publication in Applied Physics Letters (Johnson, Schwindt et al. 2010).

The measured baseline of our gradiometer (~ 5 mm) is small compared to the SQUID system (~ 30 mm), despite the vapor cell dimension of 25 mm. Therefore, it is unlikely that gradiometry will provide a higher signal-to-noise ratio than magnetometry in our AM because much of the signal from the neural source is common to all quadrant photodiode channels. Future designs will likely benefit from abandoning the quadrant photodiodes required for gradiometry given the difficulty of properly aligning the quadrant photodiodes compared to the simplicity of using single element photodetectors.

Although our initial MEG measurements were successful, two areas in particular were identified as needing improvement.

First, the cylindrical geometry of our coils resulted in preferentially strong field modulation capabilities along the axis of the cylinder. As a result, the fields could not be strongly modulated in the radial direction of the cylinder, resulting in the detection of significantly weaker MEG signals in the radial direction. Figure 17 illustrates the point, where the "vertical field" refers to the vertical direction in the room at MRN, and therefore the radial direction of the coil system, while the "horizontal direction" is along the axis of the coil system. The data demonstrates that repeatable signals were obtained in both directions, but it is clear that the signal-to-noise ratio on the "horizontal" data is significantly better than in the "vertical" direction. The solution to this problem is addressed in the next section.

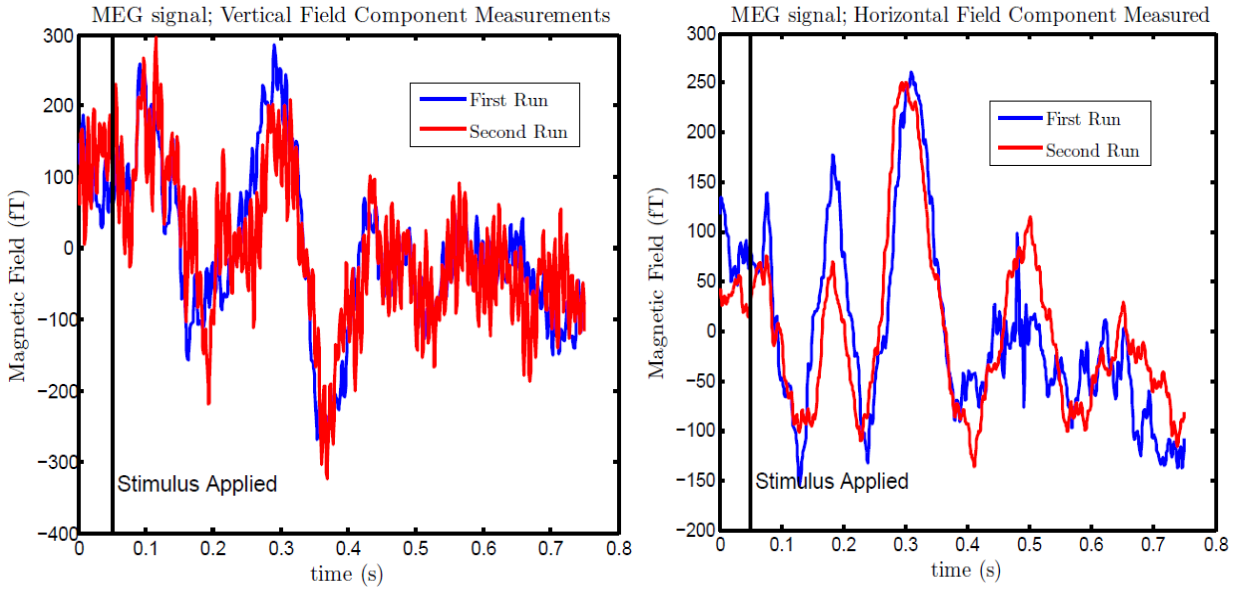

Figure 17: MEG signals from orthogonal field components. "Vertical" fields are measured by modulating in the radial direction of the coil system. Due to coil geometry, the modulation is weaker than in the "horizontal" direction (along the coil system axis), resulting in a smaller signal-to-noise ratio for the "vertical" field component.

Second, because the shielding factor is three orders of magnitude worse at MRN than in our magnetic shields at Sandia, the background noise level is significantly higher. This translated into sensitivity that was worse by a factor of between 4 to 20 during MEG measurements, depending on the direction of field modulation (see Figure 18). The noise between 10 and 40 Hz was particularly bad, which is unfortunate because this range overlaps the frequency band of greatest interest for MEG signals (< 100 Hz). The noise was present on both our magnetometer and the Elekta SQUID magnetometers, but can be eliminated from the SQUID data by use of advance signal processing technique available to large magnetometer arrays (as described in the next section). We could not identify the source of the noise, but did determine it was not due to our apparatus. The ultimate solution to this problem is to purchase a set of multi-layer cylindrical μ-metal shields that can accommodate a human subject, similar to the shields used in previous atomic magnetometer MEG demonstration (Xia, Baranga et al. 2006).

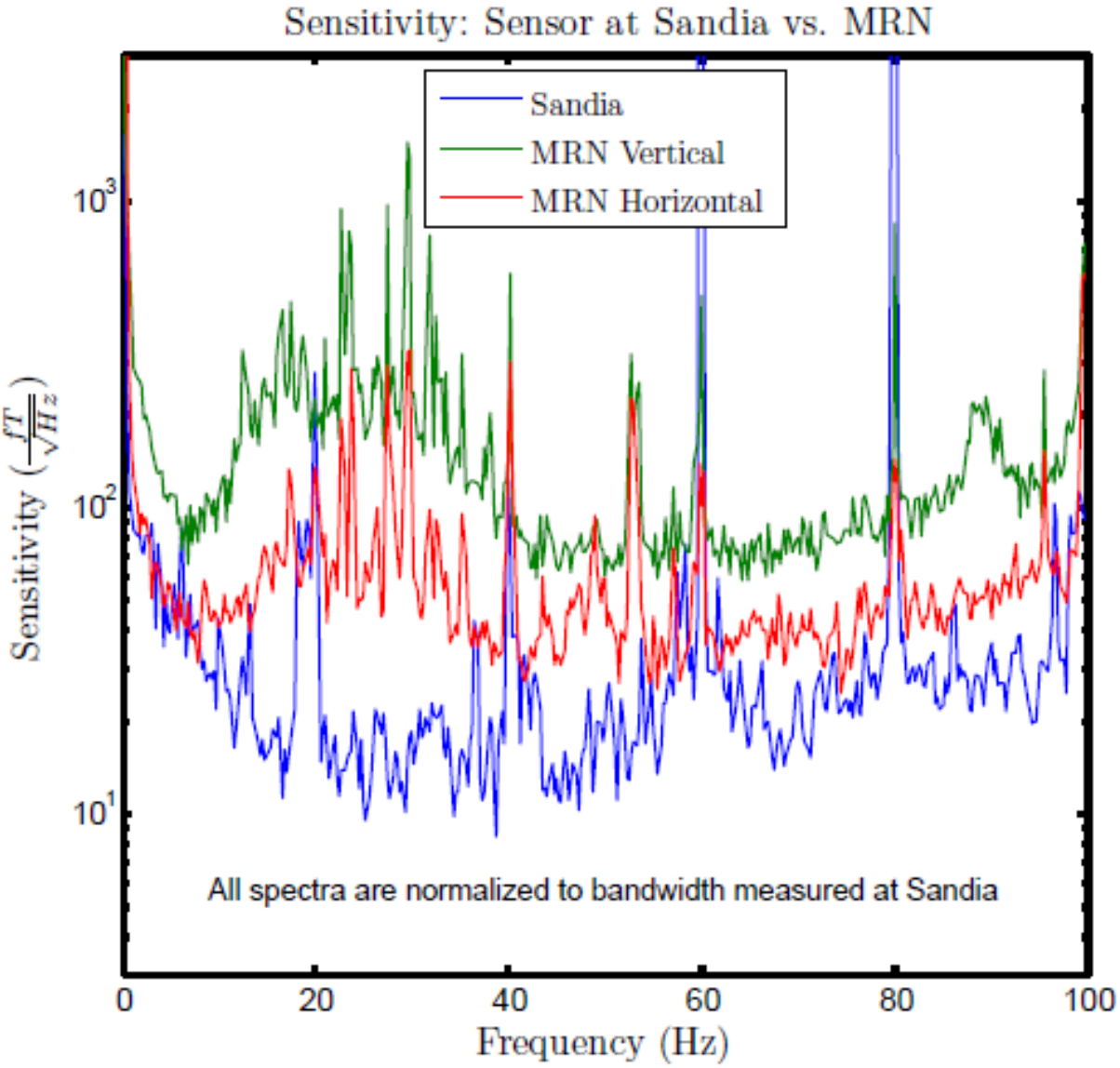

Figure 18: Measured single channel sensitivity at Sandia and MRN

4.3 Multiple Sensor MEG measurements

After our initial success with a single sensor, the goal the final phase of the project was to demonstrate the first step toward a whole-head sensor array by making MEG measurements with two simultaneously operating sensors.

Operating multiple sensors requires that DC magnetic fields are zeroed to less than one nanotesla in multiple locations and that field modulations can be applied perpendicular to the optical axes of each sensor. Although our 18-coil system was designed to produce a uniform field over a large area, our 18-channel current supply system had problems in that not all channels functioned properly. To reduce the number of channels required to operate the coils, we paired the smaller square coil that were opposite to each other on the cylinder forming the coil structure. This reduced the number of channels for the square coils from 16 to 8 so that the overall number of channels was 10. The limited field control did not allow us to control gradients within the coil system. This coupled with the fact that our coil system was unable to provide sufficient modulation in the vertical direction led us to seek a different solution to zero the field at each sensor and provide the required modulation in the form of coils wrapped directly on the vacuum enclosure of the sensor.

The on-sensor coils were designed to give the most uniform field possible over the volume of the vapor cell given the geometrical constraints of the vacuum enclosure. The sides of the square tube of the vacuum enclosure had a length of 6.3 cm and the center of the cell was roughly 2.4 cm from the end of the enclosure. This gave a coil with dimensions of 6.2 cm by 4.8 cm glued to four sides of the enclosure (Figures 19 and 20). When coils on opposite sides of the sensor are driven together, they produce a fairly uniform field, but the uniformity can be improved by placing a smaller coil inside of the larger coil with an equal current passing in the opposite direction. The dimensions of this inner coil were numerically determined by minimizing the second derivative of the field at the center of the cell. This minimization gave dimension of 3.7 cm by 1.4 cm to the smaller coil. With the coil pair shown in Figure 19 glued to the four sides of the vacuum enclosure, we could control the transverse fields at each vapor cell. To control the longitudinal field we wrapped square Helmholtz coils (not shown in Figure 19) around the vacuum enclosure. Using the on-sensor coils to provide the magnetic field modulation required to operate the magnetometer, we saw no change in the magnetometer sensitivity when measured in the 4-layer shield at Sandia.

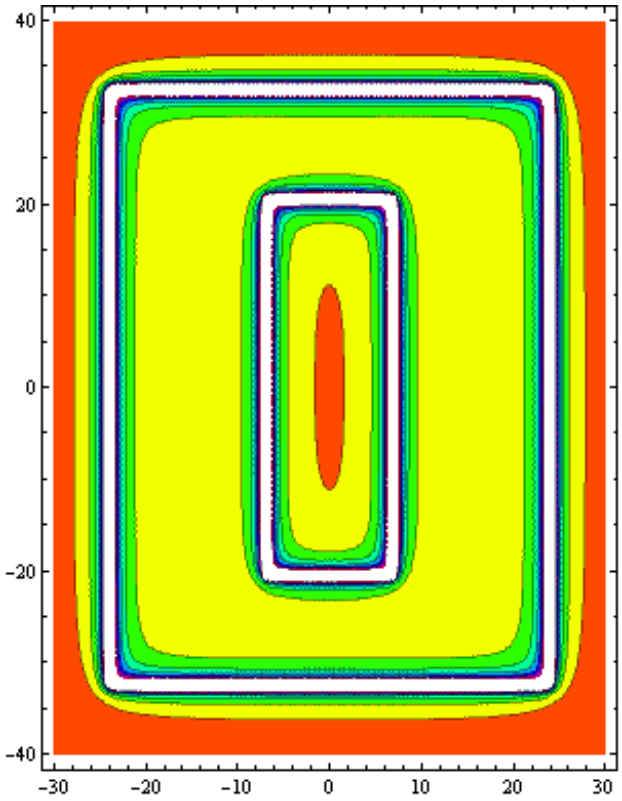

Figure 19: Contour plot of the magnitude of the magnetic field in the plane of the large and small coil pair. The white lines show the positions of the coils. The dimensions of the axes are in millimeters.

Our final protocol for controlling the fields at the two sensors was to use the large 18-coil system to zero the field at one of the sensors. Then, we adjusted the currents to the on-sensor coils on the second sensor to zero the fields there. The DC fields were zeroed as measured by the magnetometers. With the fields zeroed, we could the select sensitive axis of the magnetometers by applying the appropriate 1.1 kHz modulation to the appropriate on-sensor coils. This technique provided sufficient modulation for optimal operation of the magnetometers in both the vertical and horizontal sensitivity directions. This is a clear improvement over our single sensor data run where only the large coil system was used to produce the modulated field. (Because the pump laser was not tuned directly on resonance, it produced a light shift along the optical axis which acts as a fictitious magnetic field along the longitudinal direction. The applied longitudinal field compensates for this fictitious field, and therefore the actual field was not truly at zero.)

Figure 20 shows a human subject prepared for auditory stimuli MEG measurements. Sensors have been mounted on opposite sides of the head over each auditory cortex. The on-sensor coils near the head (in the vicinity of the vapor cell) are visible.

Figure 20: Subject prepared for multi-sensor auditory stimuli MEG measurements.

As we made single-sensor measurements it was noted that the ambient field noise from 10-40 Hz was much larger at MRN than in our shields at Sandia. However, this noise averaged down sufficiently well to detect the clear signals presented in Section 4.2. Unfortunately, the noise did not average away as effectively while we took two-sensor. Attempts at filtering the offending noise band were of limited use because it was found that noise common to both sensors was dominant unless the data was low-pass filtered at 10 Hz. This filtering is too aggressive compared to the expected MEG signal bandwidth, and much of the expected signal is also lost.

Fortunately, by using more than one sensor, it is possible to use signal processing techniques to distinguish ambient magnetic field noise from signal from the brain. This can be achieved because ambient magnetic field noise will in general be fairly uniform over sensors arrayed around a subject's head whereas the fields produced by sources within the brain will have a high degree of spatial variation. A signal processing technique often used in SQUID-based whole-head MEG arrays is signal space projection (Uusitalo and Ilmoniemi 1997). As an example of this technique, with a 300-sensor system, a 300-dimensional signal space is defined. The ambient magnetic field is measured without a subject in the device, and the ambient field defines a small number of ambient field vectors in the 300-dimensional space. These vectors are independent of how the ambient field fluctuates over time. With these vectors defined, any measured signal

parallel to these vectors in the signal space can be subtracted since it is known to be ambient magnetic field. In large scales arrays, signal space projection can reduce ambient fields by a factor of 1000, and the ambient field vectors are stable over long periods (years).

Because the two sensors were separated by 20 cm in our two-sensor measurements, ambient field and field from the brain likely produced fields that are proportionally different at the two sensors, and a technique like signal space projection could eliminate a large portion of the magnetic field noise. (We did not use signal space projection or related techniques with our single sensor data because the four channels in the sensor are too closely spaced.) However, we did not use signal space projection because it requires measurements of field noise prior to human subject measurements. Our system is likely not stable enough for the signal space vector of the field noise to be valid after the subject is in the system because our sensors are not rigidly mounted and would be in a different position before and after subject installation. Also, the gain of our sensors seems to have a long-term drift that would affect the direction of the noise vector in signal space over time. Therefore, we used a different technique call principal component analysis (PCA). PCA is similar to signal space projection in that vectors in signal space are identified, but the analysis is done only with the MEG data from the human subject and does not use any prior measurements. With our two sensor measurements, we had a total of 8 channels of data, defining an 8-dimensional space. PCA identifies the principle directions in the signal space along which most of the data is aligned. Typically most of the signal power lies along only two or three orthogonal components, and PCA defines these components and ranks them.

In our case, the largest signal was from the ambient magnetic field noise while the signal from the brain was much smaller. This was evident because the averaged signal over all stimuli looked similar for both sensors, implying both sensors experienced similar fields during the measurement; this is only possible if the primary signal strength is due to noise common to both sensors. Thus, in the data analysis of the MEG signals, we assume the strongest principal component identified in PCA is from the ambient field and the signal along this direction was therefore removed from the data. The remaining data were then analyzed in the typical way by averaging evoked response epochs together. Our assumption that the largest principal component is due to the ambient field is supported by the auditory data plotted in Figure 21. A visual inspection of the raw data (averaged over all stimuli) for sensor 1 and sensor 2 reveals that most of the signal is common to both sensors throughout the data acquisition (although of opposite sign in Figure 21). The principal component is found to look similar to noise common to both sensors, demonstrating that the common mode noise is indeed along the principal component. However, its magnitude ought not to be compared to the raw signals because it is in a different basis. After the principal component is removed, the signal-to-noise ratio on the processed single-channel signal is clearly higher than the raw data. The filtering of data in Figure 21 is identical to the 1-40 Hz filtering used on the single sensor data presented in Section 4.2. Because our signal space has only 8 dimensions, it is highly likely that some of the MEG signal is contained in the largest principal component and is then eliminated when this component is removed from the data. As a signal space gets larger with more sensors added to the array, this becomes less of a problem because ambient field and MEG signal become more widely separated in the signal space.

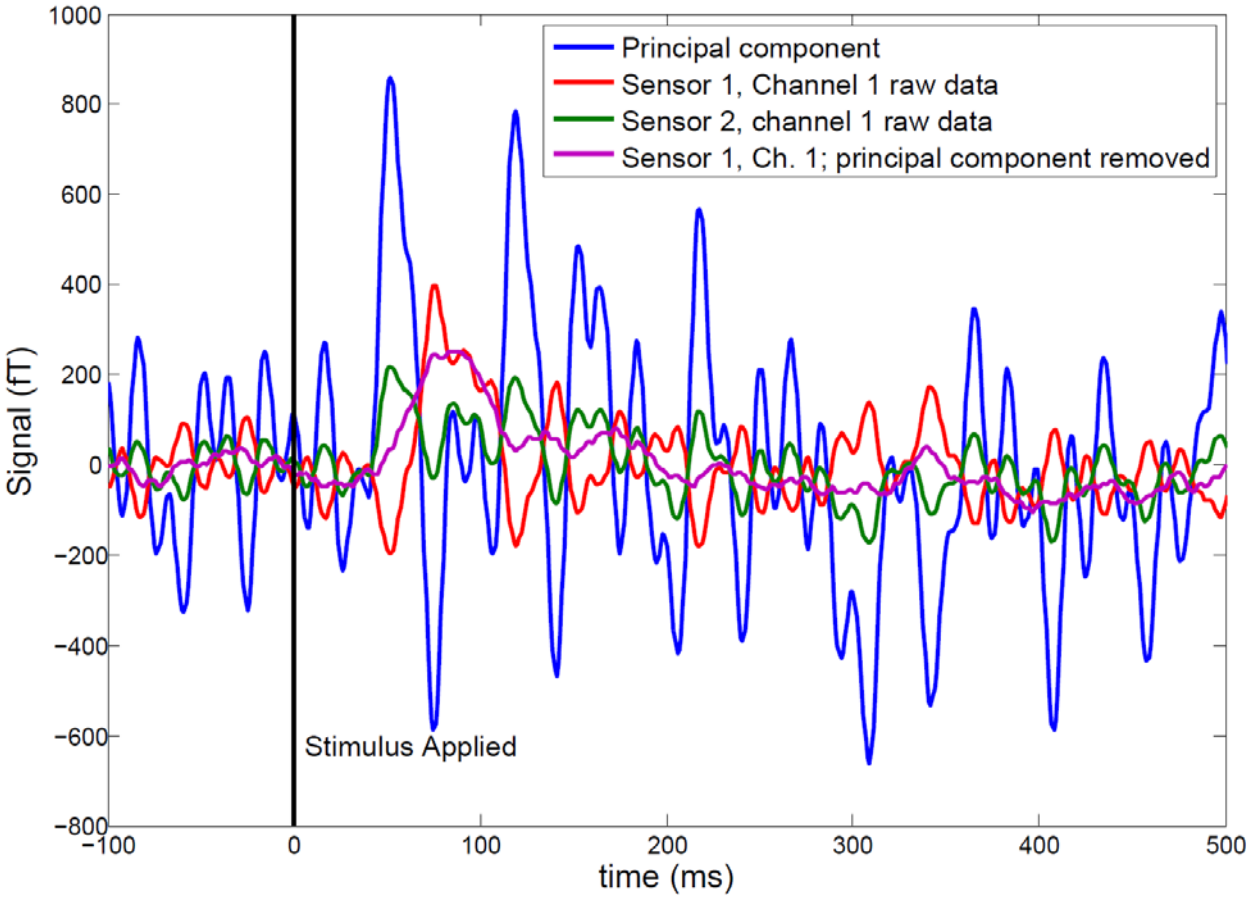

Figure 21: Comparison of raw data from both sensors, the principal component found using both sensors' data, and single channel data with principal component removed. The magnitude of the principal component ought not to be directly compared to the raw signals because it is in a different basis.

During the multi-sensor data run, auditory data was taken on three human subjects and median nerve stimulation was performed on two subjects. No additional SQUID MEG data was taken. Auditory stimuli were presented exactly as described above for single-sensor MEG measurements. Median nerve stimuli were presented every 2 +/- 0.5 ms. Figure 22 shows data taken without a human subject in the shielded room but with 2000 Hz auditory tones presented at the location of the sensors. This measurement was taken with the horizontal sensitivity axis activated. Figure 23 shows data taken with a human subject in the room and median nerve stimulation electrodes positioned on the wrist, but without being properly placed to elicit a twitch in the thumb. The auditory data is particularly low noise (typically < 20 fT) while the somatosensory data is slightly more noisy, but still less than ~ 40 fT. Figures 22 and 23 are baselines for comparison with MEG data taken while stimulations were presented to human subjects.

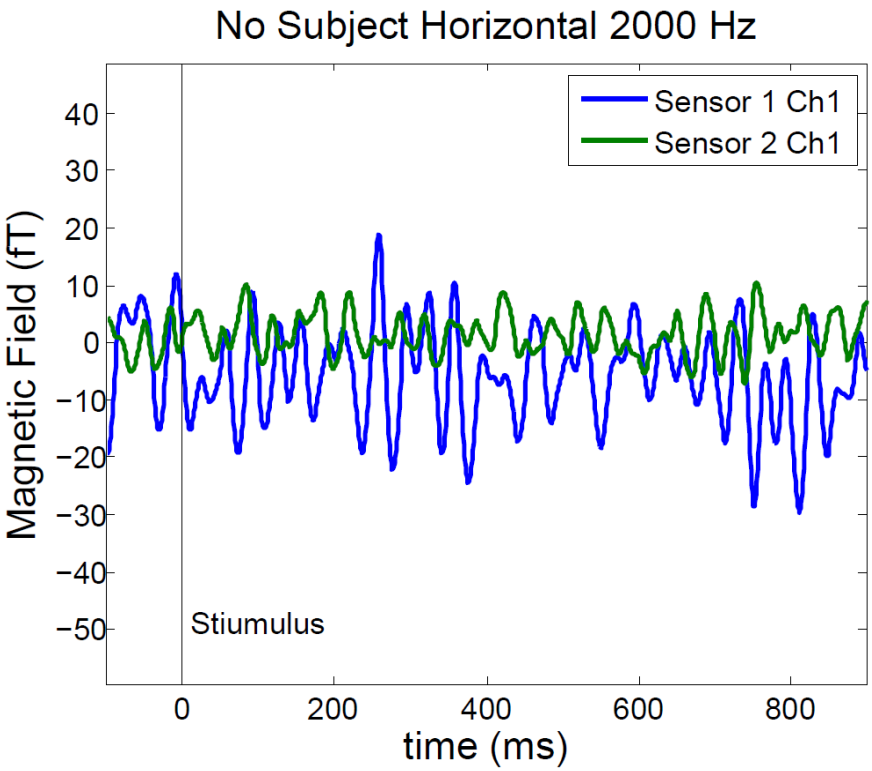

Figure 22: Data taken with no subject in MEG apparatus. The field sensitivity axis is horizontal and auditory tones of 2000 Hz were presented at the sensors.

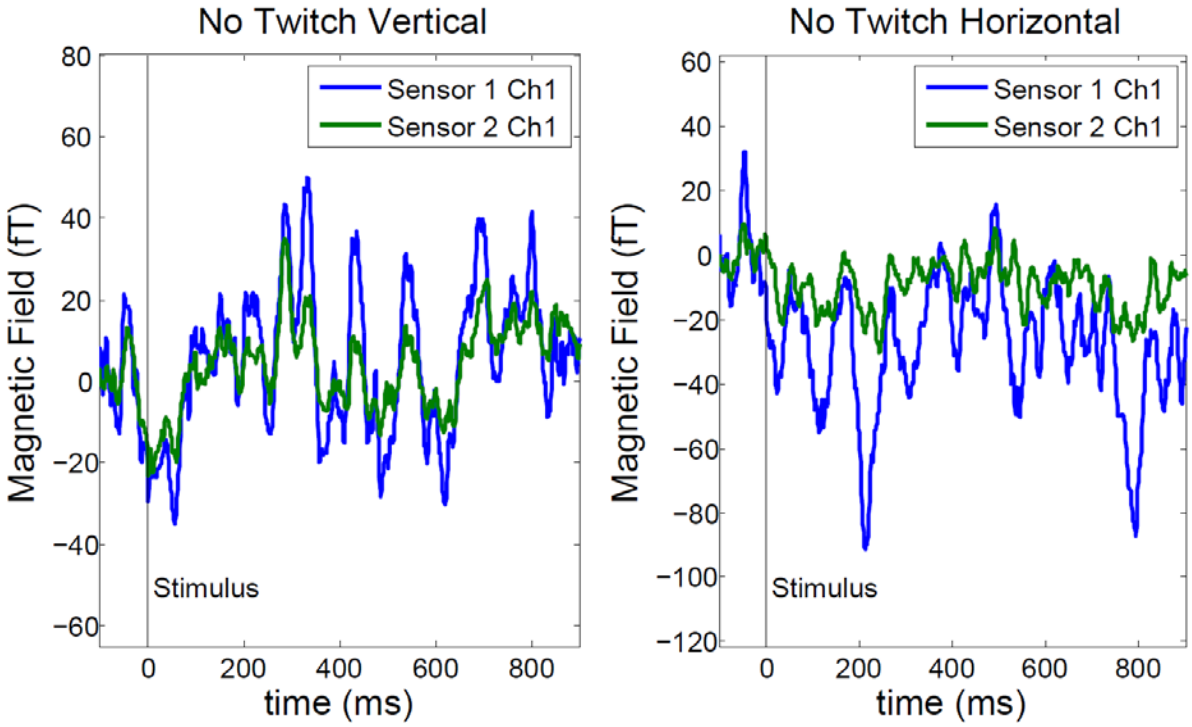

Figure 23: Median nerve data taken in both horizontal and vertical sensitivity modes; electrode arranged to produce no wrist twitch on human subject.

On the following pages, the data taken for each subject in each modality is displayed. Most of the plots are significantly different from Figure 22 and 23, indicating measured signals from the brain.

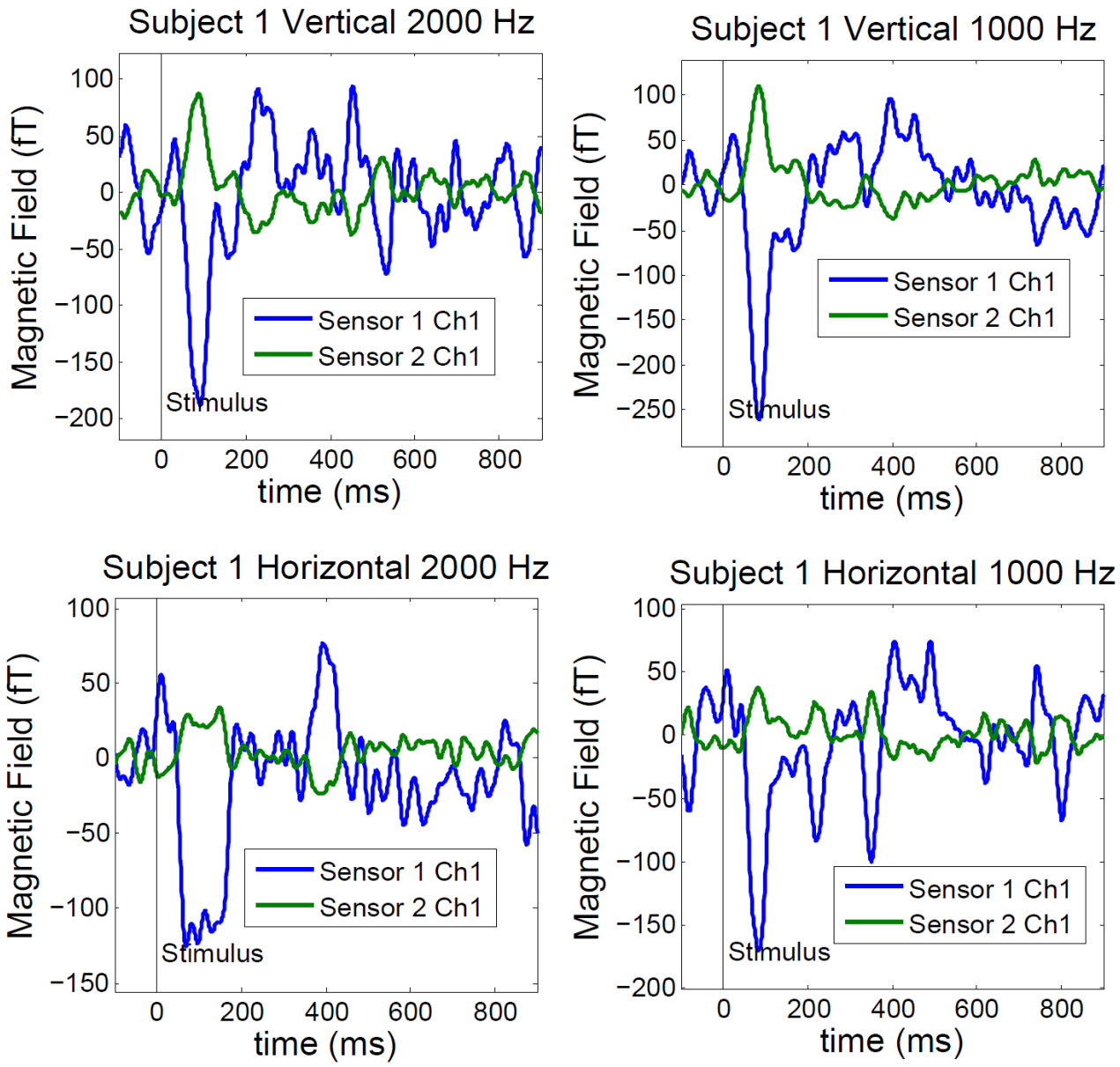

Figure 24: Auditory data for Subject 1 for 1000 Hz and 2000 Hz tones in both the vertical and horizontal sensitive axis configurations.

The data in Figure 24 is taken from the same subject as was used in the single-sensor measurements. In each plot, the expected auditory signal ~ 90 ms after the stimuli is visible. For an unknown reason, sensor 2 (near the right ear) signals are consistently smaller than sensor 1 (near the left ear) signals.

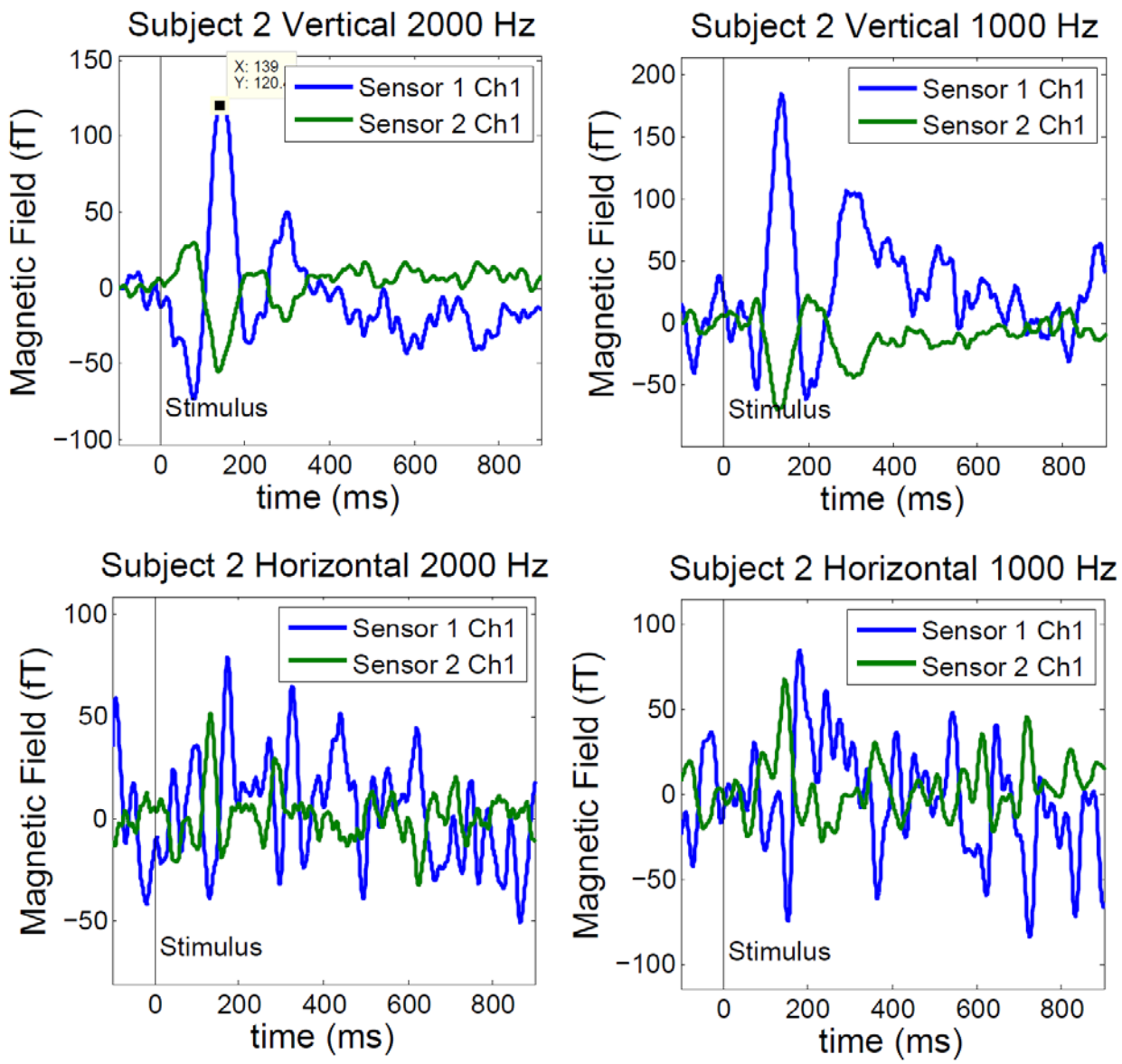

Figure 25: Auditory data for Subject 2.

In Figure 25, a clear spike is visible for vertical sensitivity at around 140 ms after the stimuli, but no apparent signal is found for horizontal sensitivity. As in Figure 24, sensor 2 signals are consistently smaller than sensor 1 signals.

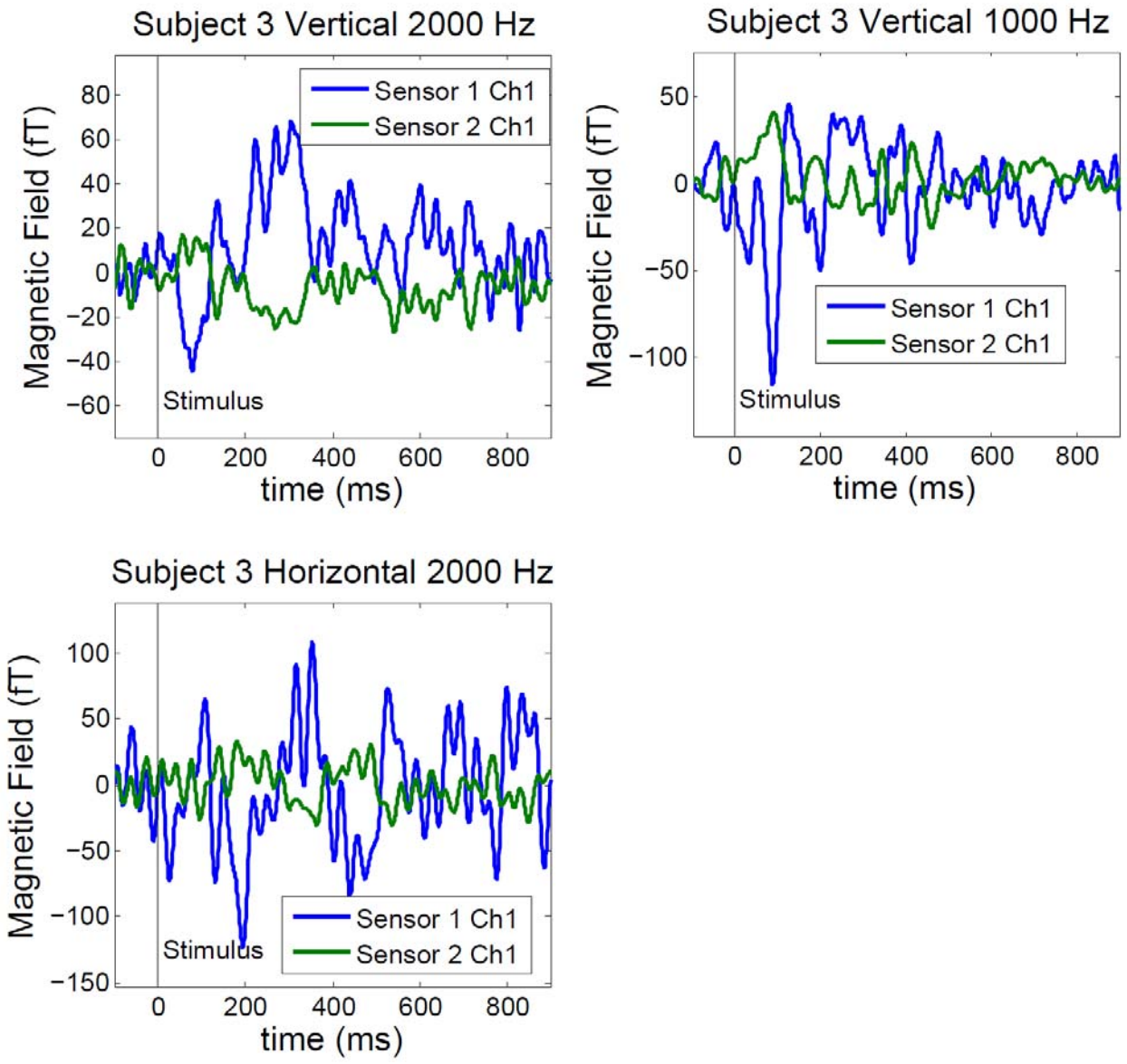

Figure 26: Auditory data for Subject 3.

In Figure 26, data taken with horizontal sensitivity and 1000 Hz tones was corrupted and is not available. Auditory signals are much less clear from Subject 3, which is qualitatively consistent with auditory MEG scans previously taken on Subject 3 using the Elekta SQUID apparatus.

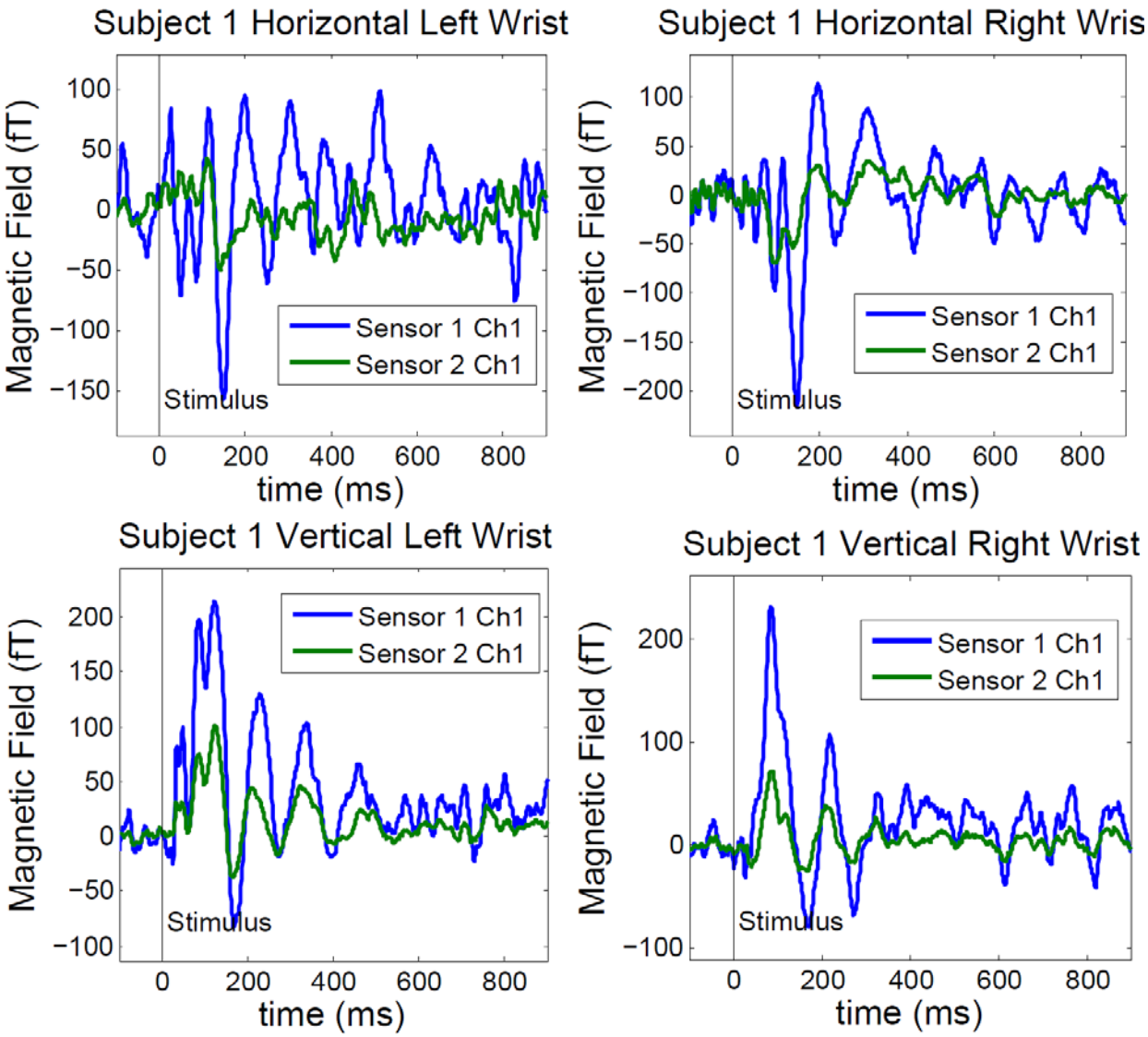

Figure 27: Somatosensory data for Subject 1

When the left wrist is stimulated, it is expected that signals will be stronger on the right side of the head (sensor 1) and vice versa for right wrist stimulation. This behavior is not obviously demonstrated in Figure 27. While signals in the first 500 ms are clearly visible, only the signals in the first 100 ms are routinely used in neuroscience research. Because there are no consistent, large signals in the first 100 ms, an increase in bandwidth may benefit somatosensory scans in particular.

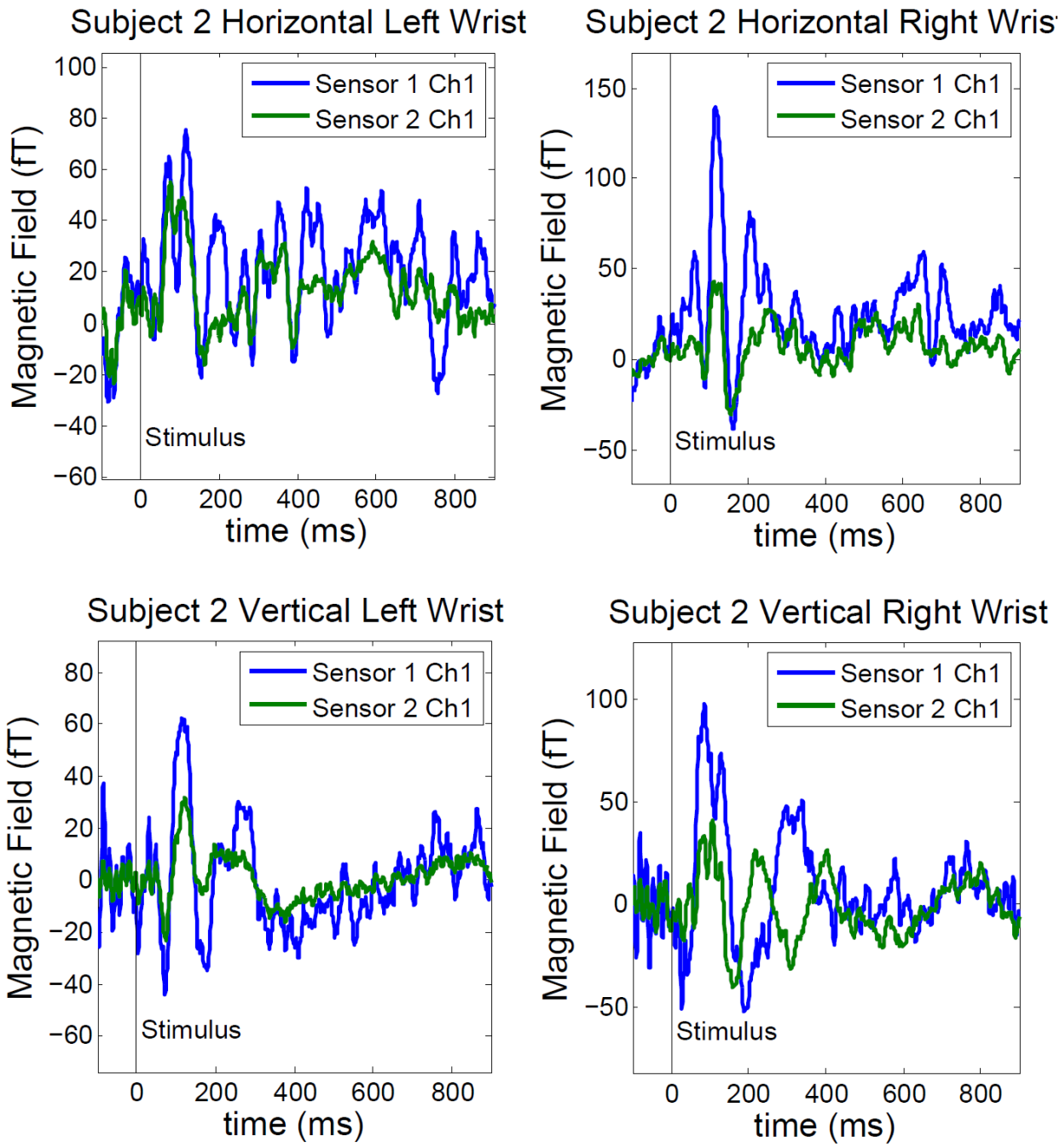

Figure 28: Somatosensory data for Subject 2

As with Figure 27, somatosensory measurements from a second subject (see Figure 28) clearly demonstrate signals in the first 500 ms, but none that are consistently large in the first 100 ms, indicating that an increase in bandwidth will benefit future somatosensory MEG scans.

Our multi-sensor MEG measurements were successful on many fronts. First, we demonstrated that by wrapping coils directly onto each sensor it was possible to both zero the ambient field at both sensors and to produce signals with equal sensitivity in both the vertical and horizontal directions. We detected clear signals from multiple subjects in both the auditory and somatosensory modalities. While the signals did vary between subjects, these differences can be physiological in nature and do not necessarily imply unreliable sensors. The auditory data in particular is most similar to the expected response from a SQUID MEG system. Improvements in bandwidth will be needed before scaling up the system into a whole-head system if somatosensory data with atomic magnetometers is to become reliable as a neuroscience tool.

5. SUMMARY AND CONCLUSIONS

We have developed a compact, fiber-coupled, multi-channel SERF magnetometer tailored to the detection of magnetic fields produced by the human brain. Our unique magnetometry scheme optically pumps a ^{87}Rb vapor cell on the D1 transition at 795 nm and probes the external magnetic field via Faraday rotation of light tuned near the D2 transition at 780 nm. Using this scheme we have constructed a compact magnetometer in which the pump and probe beams share a single optical axis while allowing independent manipulation of pump/probe parameters for magnetometer optimization. The single-axis geometry enables a simple optical design, resulting in a compact, fiber-coupled magnetometer in which the distance between the center of the active sensing volume and the head of a human subject is ~ 2 cm. The intrinsic sensitivity has been measured to be < 5 fT/rtHz. Further optimization of sensitivity and bandwidth is possible by operating the vapor cell at temperatures higher than possible given the material properties in the current design. MEG measurements on human subjects have been performed using both median nerve and auditory stimulus modalities. Atomic magnetometer measurements of a single adult male subject compare favorably with SQUID-based MEG measurements. Because the sensors are fiber-coupled, we were able to perform AM MEG with two sensors located on opposite sides of the head; the first step toward whole-head MEG.

The investment by Sandia's Laboratory Directed Research and Development office in this project has resulted in a framework for a low-cost, whole-head MEG system capable of functional imaging and source localization of neural activity. Future progress in the field will require sensors to be densely arrayed around the head. This will require miniaturization, which should be easily accomplished by using a smaller vapor cell. Although on-sensor coils worked well to zero fields and provide field modulation for both sensors in our multi-sensor measurements, as the density of sensors is increased the potential for cross-talk between sensors becomes likely. Therefore, much of the scale-up effort will be focused on determining the optimal coil configuration that will provide localized field modulations and minimize cross-talk between neighboring sensors.

REFERENCES

Allred, J. C., R. N. Lyman, et al. (2002). "High-Sensitivity Atomic Magnetometer Unaffected by Spin-Exchange Relaxation." Phys. Rev. Lett. **89**(13): 130801.

Belfi, J., G. Bevilacqua, et al. (2007). "Cesium coherent population trapping magnetometer for cardiosignal detection in an unshielded environment." J. Opt. Soc. Am. B **24**(9): 2357-2362.

Bison, G., N. Castagna, et al. (2009). "A room temperature 19-channel magnetic field mapping device for cardiac signals." Applied Physics Letters **95**(17).

Dang, H. B., A. C. Maloof, et al. (2010). "Ultrahigh sensitivity magnetic field and magnetization measurements with an atomic magnetometer." Applied Physics Letters **97**(15): 151110-151113.

Hämäläinen, M., R. Hari, et al. (1993). "Magnetoencephalography--theory, instrumentation, and applications to noninvasive studies of the working human brain." Rev. Mod. Phys. **65**(2): 413-497.

Happer, W. and H. Tang (1973). "Spin-Exchange Shift and Narrowing of Magnetic Resonance Lines in Optically Pumped Alkali Vapors." Phys. Rev. Lett. **31**(5): 273-276.

Johnson, C. and P. D. D. Schwindt (2010). A two-color pump probe atomic magnetometer for magnetoencephalography. Proc. IEEE Intl. Freq. Cont. Symp. Newport Beach, CA, USA**:** 371-375.

Johnson, C., P. D. D. Schwindt, et al. (2010). "Magnetoencephalography with a two-color pump-probe, fiber-coupled atomic magnetometer."

Knappe, S., T. H. Sander, et al. (2010). "Cross-validation of microfabricated atomic magnetometers with superconducting quantum interference devices for biomagnetic applications." Applied Physics Letters **97**(13): 133703-133703.

Kominis, I. K., T. W. Kornack, et al. (2003). "A subfemtotesla multichannel atomic magnetometer." Nature **422**: 596-599.

Ressler, N. W., R. H. Sands, et al. (1969). "Measurement of Spin-Exchange Cross Sections for ^{133}Cs, ^{87}Rb, ^{85}Rb, ^{39}K, and ^{23}Na." Phys. Rev. **184**(1): 102-118.

Shah, V. and M. V. Romalis (2009). "Spin-exchange relaxation-free magnetometry using elliptically polarized light." Phys. Rev. A **80**(1): 013416.

Uusitalo, M. and R. Ilmoniemi (1997). "Signal-space projection method for separating MEG or EEG into components." Medical and Biological Engineering and Computing **35**(2): 135-140.

Xia, H., A. B.-A. Baranga, et al. (2006). "Magnetoencephalography with an atomic magnetometer." Applied Physics Letters **89**(21): 211104.

DISTRIBUTION

1	MS1082	Cort Johnson	1725 (electronic copy)
1	MS1082	Peter Schwindt	1725 (electronic copy)
1	MS1082	Michael Descour	1725 (electronic copy)
1	MS1188	Ann Speed	1434 (electronic copy)
1	MS1188	John Wagner	1432 (electronic copy)
1	MS0899	Technical Library	9536 (electronic copy)
1	MS0359	D. Chavez, LDRD Office	1911


Sandia National Laboratories